Atmospheric
Chemistry
and Physics

Global impact of COVID-19 restrictions on the surface concentrations of nitrogen dioxide and ozone

Christoph A. Keller[1,2], Mathew J. Evans[3,4], K. Emma Knowland[1,2], Christa A. Hasenkopf[5], Sruti Modekurty[5], Robert A. Lucchesi[1,6], Tomohiro Oda[1,2], Bruno B. Franca[7], Felipe C. Mandarino[7], M. Valeria Díaz Suárez[8], Robert G. Ryan[9], Luke H. Fakes[3,4], and Steven Pawson[1]

[1]NASA Global Modeling and Assimilation Office, Goddard Space Flight Center, Greenbelt, MD, USA
[2]Universities Space Research Association, Columbia, MD, USA
[3]Wolfson Atmospheric Chemistry Laboratories, Department of Chemistry, University of York, York, YO10 5DD, UK
[4]National Centre for Atmospheric Science, University of York, York, YO10 5DD, UK
[5]OpenAQ, Washington, D.C., USA
[6]Science Systems and Applications, Inc., Lanham, MD, USA
[7]Municipal Government of Rio de Janeiro, Rio de Janeiro, Brazil
[8]Secretaria de Ambiente, Quito, Ecuador
[9]School of Earth Sciences, The University of Melbourne, Melbourne, Australia

Correspondence: Christoph A. Keller (christoph.a.keller@nasa.gov)

Abstract. Social distancing to combat the COVID-19 pandemic has led to widespread reductions in air pollutant emissions. Quantifying these changes requires a business-as-usual counterfactual that accounts for the synoptic and seasonal variability of air pollutants. We use a machine learning algorithm driven by information from the NASA GEOS-CF model to assess changes in nitrogen dioxide (NO_2) and ozone (O_3) at 5756 observation sites in 46 countries from January through June 2020. Reductions in NO_2 coincide with the timing and intensity of COVID-19 restrictions, ranging from 60 % in severely affected cities (e.g., Wuhan, Milan) to little change (e.g., Rio de Janeiro, Taipei). On average, NO_2 concentrations were 18 (13–23) % lower than business as usual from February 2020 onward. China experienced the earliest and steepest decline, but concentrations since April have mostly recovered and remained within 5 % of the business-as-usual estimate. NO_2 reductions in Europe and the US have been more gradual, with a halting recovery starting in late March. We estimate that the global NO_x (NO + NO_2) emission reduction during the first 6 months of 2020 amounted to 3.1 (2.6–3.6) TgN, equivalent to 5.5 (4.7–6.4) % of the annual anthropogenic total. The response of surface O_3 is complicated by competing influences of nonlinear atmospheric chemistry. While surface O_3 increased by up to 50 % in some locations, we find the overall net impact on daily average O_3 between February–June 2020 to be small. However, our analysis indicates a flattening of the O_3 diurnal cycle with an increase in nighttime ozone due to reduced titration and a decrease in daytime ozone, reflecting a reduction in photochemical production.

The O_3 response is dependent on season, timescale, and environment, with declines in surface O_3 forecasted if NO_x emission reductions continue.

1 Introduction

The stay-at-home orders imposed in many countries during the Northern Hemisphere spring of 2020 to slow the spread of the severe acute respiratory syndrome coronavirus 2 (SARS-CoV-2, hereafter COVID-19) led to a sharp decline in human activities across the globe (Le Quéré et al., 2020). The associated decrease in industrial production, energy consumption, and transportation resulted in a reduction in the emissions of air pollutants, notably nitrogen oxides (NO_x = NO + NO_2) (Liu et al., 2020a; Dantas et al., 2020;

Petetin et al., 2020; Tobias et al., 2020; Le et al., 2020). NO_x has a short atmospheric lifetime and are predominantly emitted during the combustion of fossil fuel for industry, transport, and domestic activities (Streets et al., 2013; Duncan et al., 2016). Atmospheric concentrations of nitrogen dioxide (NO_2) thus readily respond to local changes in NO_x emissions (Lamsal et al., 2011). While this may provide both air quality and climate benefits, a quantitative assessment of the magnitude of these impacts is complicated by the natural variability of air pollution due to variations in synoptic conditions (weather), seasonal effects, and long-term emission trends, as well as the nonlinear responses between emissions and concentrations. Thus, simply comparing the concentration of pollutants during the COVID-19 period to those immediately beforehand or to the same period in previous years is not sufficient to indicate causality. An emerging approach to address this problem is to develop machine-learning-based "weather-normalization" algorithms to establish the relationship between local meteorology and air pollutant surface concentrations (Grange et al., 2018; Grange and Carslaw, 2019; Petetin et al., 2020). By removing the meteorological influence, these studies have tried to better quantify emission changes as a result of a perturbation.

Here, we adapt this weather-normalization approach to not only include meteorological information but also compositional information in the form of the concentrations and emissions of chemical constituents. Using a collection of surface observations of NO_2 and ozone (O_3) from across the world from 2018 to July 2020 (Sect. 2.1), we develop a "bias-correction" methodology for the NASA global atmospheric composition model GEOS-CF (Sect. 2.2), which corrects the model output at each observational site based on the observations for 2018 and 2019 (Sect. 2.3). These biases reflect errors in emission estimates, sub-grid-scale local influences (representational error), or meteorology and chemistry. Since the GEOS-CF model makes no adjustments to the anthropogenic emissions in 2020, and no 2020 observations are included in the training of the bias corrector, the bias-corrected model (hereafter BCM) predictions for 2020 represent a business-as-usual scenario at each observation site that can be compared against the actual observations. This allows the impact of COVID-19 containment measures on air quality to be explored, taking into account meteorology and the long-range transport of pollutants. We first apply this to the concentration of NO_2 (Sect. 3.1) and then O_3 (Sect. 3.2) and explore the differences between the counterfactual prediction and the observed concentrations. In Sect. 3.3, we explore how the observed changes in the NO_2 concentrations relate to emission of NO_x, and in Sect. 3.4 we speculate what the COVID-19 restrictions might mean for the second half of 2020.
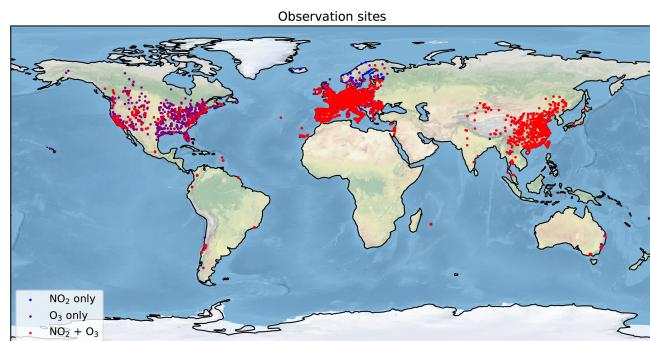

Figure 1. Location of the 5756 observation sites included in the analysis. Red points indicate sites with both NO_2 and O_3 observations (3485 in total), purple points show locations with O_3 observations only (978 sites), and blue points show locations with NO_2 observations only (1293 sites). See the Appendix for detailed maps for North America, Europe, and China.

2 Methods

2.1 Observations

Our analysis builds on the recent development of unprecedented public access to air pollution model output and air quality observations in near-real time. We compile an air quality dataset of hourly surface observations for a total of 5756 sites (4778 for NO_2 and 4463 for O_3) in 46 countries for the time period 1 January 2018 to 1 July 2020, as summarized in Fig. 1 and Table 1. More detailed maps of the spatial distribution of observation sites over China, Europe, and North America are given in Figs. A1–A3. The vast majority of the observations were obtained from the OpenAQ platform and the air quality data portal of the European Environment Agency (EEA). Both platforms provide harmonized air quality observations in near-real time, greatly facilitating the analysis of otherwise disparate data sources. For the EEA observations, we use the validated data (E1a) for the years 2018–2019 and revert to the real-time data (E2a) for 2020. For Japan, we obtained hourly surface observations for a total of 225 sites in Hokkaido, Osaka, and Tokyo from the Atmospheric Environmental Regional Observation System (AEROS) (MOE, 2020). To improve data coverage in under-sampled regions, we also included observations from the cities of Rio de Janeiro (Brazil), Quito (Ecuador), and Melbourne (Australia). All cities offer continuous, hourly observations of NO_2 and O_3 over the full analysis period, thus offering an excellent snapshot of air quality at these locations. We include all sites with at least 365 d of observations between 1 January 2018 and 31 December 2019 and an overall data coverage of 75 % or more since the first day of availability. Only days with at least 12 h of valid data are included in the analysis. The final NO_2 and O_3 dataset comprise 8.9×10^7 and 8.2×10^7 hourly observations, respectively.

Table 1. Observational data sources used in the analysis. Time period covers 1 January 2018–1 July 2020.

Name	Countries	Sites	Source
OpenAQ	Australia, China, India, Hong Kong, Taiwan, Thailand, Canada, Chile, Colombia, United States	2410	https://openaq.org/ (last access: 3 July 2020)
EEA	Austria, Belgium, Bosnia and Herzegovina, Bulgaria, Croatia, Cyprus, Czech Republic, Denmark, Estonia, Finland, France, Germany, Greece, Hungary, Iceland, Ireland, Italy, Latvia, Lithuania, Luxembourg, North Macedonia, Malta, Netherlands, Norway, Poland, Portugal, Romania, Serbia, Slovakia, Slovenia, Spain, Sweden, Switzerland, United Kingdom	3101	https://discomap.eea.europa.eu/map/fme/AirQualityExport.htm (last access: 3 July 2020)
AEROS	Japan	225	http://soramame.taiki.go.jp/Index.php (last access: 4 July 2020)
EPA Victoria	Australia (Melbourne)	4	http://sciwebsvc.epa.vic.gov.au/aqapi/Help (last access: 4 July 2020)
Secretaria de Ambiente, Quito	Ecuador (Quito)	8	http://www.quitoambiente.gob.ec/ambiente/index.php (last access: 4 July 2020)
Municipal Government of Rio de Janeiro	Brazil (Rio de Janeiro)	8	http://www.data.rio/datasets/dados-hor (last access: 4 July 2020)

2.2 Model

Meteorological and atmospheric chemistry information at each of the air quality observation sites is obtained from the NASA Goddard Earth Observing System Composition Forecast (GEOS-CF) model (Keller et al., 2020). GEOS-CF integrates the GEOS-Chem atmospheric chemistry model (v12-01) into the GEOS Earth System Model (Long et al., 2015; Hu et al., 2018) and provides global hourly analyses of atmospheric composition at $25 \times 25 \, \text{km}^2$ spatial resolution, available in near-real time at https://gmao.gsfc.nasa.gov/weather_prediction/GEOS-CF/data_access/, last access: 5 July 2020 (Knowland et al., 2020). Anthropogenic emissions are prescribed using monthly Hemispheric Transport of Air Pollution (HTAP) bottom-up emissions (Janssens-Maenhout et al., 2015), with imposed weekly and diurnal scale factors as described in Keller et al. (2020). The same anthropogenic base emissions are used for the years 2018–2020. Therefore, GEOS-CF does not account for any anthropogenic emission changes since 2018, notably any anthropogenic emission reductions related to COVID-19 restrictions. However, it does capture the variability in natural emissions such as wildfires (based on the Quick Fire Emissions Dataset, QFED) (Darmenov and Da Silva, 2015) or lightning and biogenic emissions (Keller et al., 2014). While the meteorology and stratospheric ozone in GEOS-CF are fully constrained by precomputed analysis fields produced by other GEOS systems (Lucchesi, 2015; Wargan et al., 2015), no trace gas observations are directly assimilated into the current version of GEOS-CF. It thus provides a "business-as-usual" estimate of NO_2 and O_3 that can be used as a baseline for input into the meteorological normalization process.

2.3 Machine learning bias correction

2.3.1 Overall strategy

We use the XGBoost machine learning algorithm (https://xgboost.readthedocs.io/en/latest/#, last access: 15 March 2020) (Chen and Guestrin, 2016; Frery et al., 2017) to develop a machine learning model to predict the time-varying bias at each observation site at an hourly scale. XGBoost uses the Gradient Boosting framework to build an ensemble of decision trees, trained iteratively on the residual errors to improve the model predictions in a stagewise manner (Friedman, 2001). Based on the 2018–2019 observation–model differences, the machine learning model is trained to predict the systematic (recurring) model bias between hourly observations and the co-located model predictions. These biases can be due to errors in the model, such as emission estimates, sub-grid-scale local influences (representational error), or meteorology and chemistry. Since model biases are often site-specific, we train a separate machine learning model for each site.

The design of the XGBoost framework is determined by a set of hyperparameters, such as the learning rate, maximum tree depth, or minimum loss reduction. While a full hyperparameter optimization across all sites – e.g., by using a grid search approach – would be computationally prohibitive, we conducted hyperparameter sensitivity tests at few selected sites and found that the XGBoost performance only improved marginally at these sites when using hyperparameters other than the model defaults (less than 5 % improvement). In addition, we found that the sites respond differently to the same change in hyperparameter setup, suggesting that there is no uniform hyperparameter design that is optimal across all sites. Based on this, we chose to use the default XGBoost model parameters at all locations, with a learning rate of 0.3, minimum loss reduction of 0, maximum tree depth of 6, and L1 and L2 regularization terms of 0 and 1, respectively.

For each location, we split the 2-year training dataset into eight quarterly segments (January–March, April–June, etc.) and train the model eight times, each time omitting one of the segments (8-fold cross validation). The omitted segment is used as test data to validate the general performance of the machine learning model and to provide an uncertainty estimate, as is further discussed below. This approach aims to reduce the auto-correlation signal that can lead to overly optimistic machine learning results (Kleinert et al., 2021), while still including data from all four seasons in the testing. Once trained, the final model prediction at each location consists of the average prediction of the eight models.

The observations used in this analysis are not always quality-controlled, which can cause issues if erroneous observations are included in the training, such as unrealistically high O_3 concentrations of several thousand parts per billion by volume. As an ad hoc solution to this problem, we remove all observations below or above 2 standard deviations from the annual mean from the analysis. Sensitivity tests using more stringent thresholds of 3 or even 4 standard deviations resulted in no significant change in our results.

2.3.2 Evaluation of model predictors

The input variables fed into the XGBoost algorithm are provided in Table A1. The input features encompass 9 meteorological parameters (as simulated by the GEOS-CF model: surface northward and eastward wind components, surface temperature and skin temperature, surface relative humidity, total cloud coverage, total precipitation, surface pressure, and planetary boundary layer height), modeled surface concentrations of 51 chemical species (O_3, NO_x, carbon monoxide, volatile organic compounds (VOCs), and aerosols), and 21 modeled emissions at the given location. In addition, we provide as input features the hour of the day, day of the week, and month of the year; these allow the machine learning model to identify systematic observation–model mismatches related to the diurnal, weekly, and seasonal cycle of the pollutants. In addition, for sites with observations available for the full two years, we provide the calendar days since 1 January 2018 as an additional input feature to also correct for inter-annual trends in air pollution, e.g., due to a steady decrease in emissions not captured by the model. This follows a similar technique to Ivatt and Evans (2020) and Petetin et al. (2020).

Gradient-boosted tree models consist of a tree-like decision structure, which can be analyzed to understand how the model uses the input features to make a prediction. Particularly useful in this context is the SHapely Additive exPlanations (SHAP) approach, which is based on game-theoretic Shapely values and represents a measure of each feature's responsibility for a change in the model prediction (Lundberg et al., 2017). SHAP values are computed separately for each individual model prediction, offering detailed insight into the importance of each input feature to this prediction while also considering the role of feature interactions (Lundberg et al., 2020). In addition, combining the local SHAP values offers a representation of the global structure of the machine learning model.

Figure A4 shows the distribution of the SHAP values for all NO_2 predictors separated by polluted sites (left panel) and non-polluted sites (right panel), with polluted sites defined as locations with an annual average NO_2 concentration of more than 15 ppbv. Generally, the model-predicted (unbiased) NO_2 concentration is the most important predictor for the model bias, followed by the hour of the day, the day since 1 January 2018 ("trendday"), and a suite of meteorological variables including wind speed (u10m, v10m), planetary boundary hight (zpbl), and specific humidity (q10m). All of these factors are expected to highly impact NO_2 concentrations and it is thus not surprising that the model biases are most sensitive to them. While there is considerable spread in the feature importance across the individual sites, there is little overall difference in the feature ranking between polluted vs. non-polluted sites.

Figure A5 shows the SHAP value distribution for all O_3 predictors, again separated into polluted and non-polluted sites (using the same definition as for the NO_2 sites). Unlike for NO_2, the bias-correction models for polluted sites exhibit different feature sensitivities than the non-polluted sites. At polluted locations, the availability of reactive nitrogen (NO_2, NO_y, PAN) is the dominant factor for explaining the model O_3 bias, reflecting the tight chemical coupling between NO_x and O_3 (Seinfeld and Pandis, 2016). This is followed by the month of the year, total precipitation (tprec), and O_3 concentration, again variables that are expected to be correlated to O_3. At non-polluted sites, the uncorrected O_3 concentration is on average the most relevant input feature for the bias correctors, followed by the month of the year and the odd oxygen concentration ($O_x = NO_2 + O_3$). The non-polluted sites are generally more sensitive to wind speed, reflecting the fact that O_3 production and loss at these locations is less dominated by local processes compared to the polluted sites.

2.3.3 Machine learning model skill scores

Figures 2 and 3 summarize the machine learning model statistics for NO_2 and O_3, respectively. The normalized mean bias (NMB), normalized root-mean-square error (NRMSE), and Pearson correlation coefficient (R) at each site are shown for both the training (blue) and the test (red) dataset. We define NMB as mean bias normalized by average concentration at the given site, and the NRMSE as the root-mean-square error normalized by the range of the 95th percentile concentration and 5th percentile concentration. Rather than using the mean as the denominator for the NRMSE, we choose the percentile window as a better reference point for the concentration variability at a given site. Using the mean as the denominator for the NRMSE would lead to very similar qualitative results.

For both NO_2 and O_3, the bias-corrected model predictions show no bias when evaluated against the training data, NRMSEs of less than 0.3, and correlation coefficients between 0.6–1.0 (NO_2) and 0.75–1.0 (O_3). Compared to the training data, the skill scores on the test data show a higher variability, with an average NMB of -0.047 for NO_2 and -0.034 for O_3, a NRMSE of 0.25 (NO_2) and 0.18 (O_3), and a correlation of 0.64 (NO_2) and 0.84 (O_3). We find no significant difference in skill scores between background vs. polluted sites or different countries.

A number of factors likely contribute to the poorer statistical results at some of the sites. Importantly, some sites might be prone to overfitting if the training data include events that are not easily generalizable, such as unusual emission activity (e.g., biomass burning, fireworks, closure of nearby point source) or weather patterns that are not frequently observed. In addition, the availability of test data at some locations is weak (less than 50 %), which can contribute to a poorer skill score.

2.3.4 Uncertainty estimation

To quantify the uncertainty of an individual model predictions at any given site, we use the standard deviation of the model-observation differences on the test data. For sites with 100 % test data coverage, this represents the standard deviation from a sample of 17 520 hourly model-observation pairs. The thus obtained individual NO_2 prediction uncertainties range between 3.9–28 ppbv (mean = 8.5 ppbv) at polluted sites and 0.1–18 ppbv at clean sites (average of 4.9 ppbv). On a relative basis, this corresponds to an average uncertainty of 45 % at polluted sites and 65 % at clean sites. For O_3, we obtain an average individual prediction uncertainty of 14 ppbv (4.6–33 ppbv) at polluted sites and 9.0 ppbv (2.8–45 ppbv) at clean sites, corresponding to an average relative uncertainty of an individual prediction of 29 % and 33 % at polluted and clean sites, respectively.

The results presented in this paper are averages aggregated over multiple hours and locations, and the reported uncertainties are adjusted accordingly by calculating the mean uncertainty $\overline{\sigma}$ from the above-described hourly uncertainties σ_i:

$$\overline{\sigma}^2 = \sum_{i=1}^{N} \left(\frac{\sigma_i}{N}\right)^2. \tag{1}$$

This assumes that the errors across individual sites are uncorrelated. The error covariance across sites is complex: two urban sites close to each other might show a low degree of error correlation due to local-scale (street, canyon, etc.) differences, whereas two background sites further apart might show significantly more correlation due to regional-scale (synoptic) processes. In addition, our uncertainty calculation also implies that the aggregated mean error approaches zero. Given that the average mean biases of the machine learning models are clustered around zero (Figs. 2 and 3), this is a valid general assumption – especially when aggregating across multiple sites. For simplicity we keep the current analysis but acknowledge that it might lead to overly optimistic uncertainty estimates for sites with a relatively large mean bias.

2.4 Lockdown dates

To support interpretation and guide visualizations, we include approximate national lockdown dates in all figures. The start and end dates for these are from https://en.wikipedia.org/wiki/COVID-19_pandemic_lockdowns, last access: 1 July 2020 (as of 1 July 2020) or based on local knowledge, with the full list of start and end dates given in Table A2. It should be noted that in many countries lockdown policy varied regionally and that many locations enacted "soft" stay-at-home orders before the official lockdowns. Human behavior is therefore expected to have changed considerably in many locations before the official lockdowns went into force.

3 Results

3.1 Nitrogen dioxide

Figure 4 shows the weekly mean observations of NO_2 concentration, the GEOS-CF estimate, and the BCM prediction based on the machine learning predictor trained on 2018–2019 for the five cities of Wuhan (China), Taipei (Taiwan), Milan (Italy), New York (USA), and Rio de Janeiro (Brazil) from January 2018 through June 2020. We choose these five cities for illustration as they represent a diverse level of socio-economic development and due to the cities' variable responses to the COVID-19 pandemic. These five cities are also illustrative of the varying quality of the uncorrected GEOS-CF predictions compared to the observations. For example, as shown by the dashed grey lines vs. the solid black lines in Fig. 4, the uncorrected model predictions are in good agreement with observations in Rio de Janeiro but underestimate the observed NO_2 concentrations in Taipei and Milan

**Machine learning statistics NO$_2$**
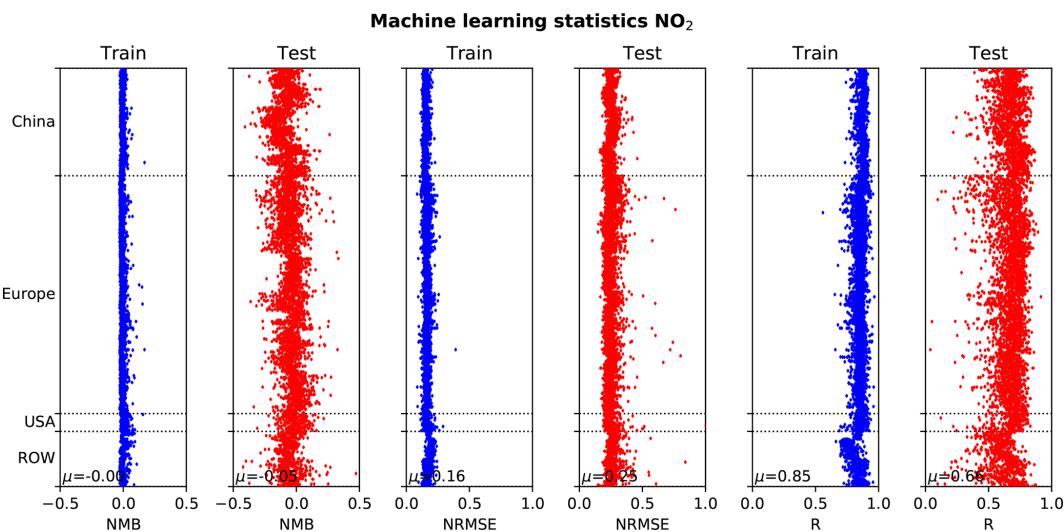
Figure 2. Machine learning statistics between hourly observations and the corresponding bias-corrected model predictions for each observation location. Shown are the normalized mean bias (NMB), normalized root-mean-square error (NRMSE), and Pearson correlation coefficient (R) for the training data (blue) and the test data (red). Data are sorted by region: China, Europe, United States (USA), and rest of the world (ROW). The mean values across all locations are shown in the figure inset.

Machine learning statistics O$_3$
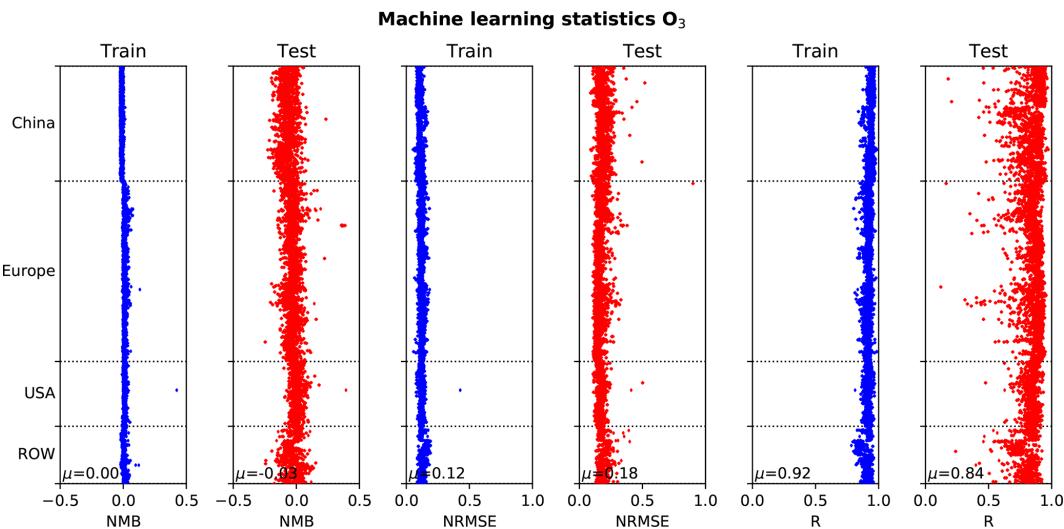
Figure 3. The same as Fig. 2 but for O$_3$.

while overestimating concentrations over New York. These differences are a combination of the observation–model scale mismatch (25×25 km^2 vs. point observation) and model errors, such as the simulated spatiotemporal distribution of NO$_x$ emissions or the modeling of the local boundary layer. The model–observation mismatch is particularly pronounced for Wuhan, where the model does not capture the observed seasonal cycle, pointing to errors in the imposed seasonal cycle of NO$_x$ emissions in the model.

In contrast to the uncorrected model predictions, the BCM closely follows the observations for years 2018 and 2019 (dashed black lines in Fig. 4). The grey region in Fig. 4 shows

the start and end of the implementation of COVID-19 containment measures. Once containment is implemented, observed concentrations start to diverge from the BCM prediction for Wuhan, Milan, and New York (Fig. 4). For Wuhan, we find a reduction in NO$_2$ of 54 (48–59) % relative to the expected BCM value for February and March 2020, and average decreases of 30 %–40 % are found over Milan (24 %–43 %) and New York (20 %–34 %) starting in mid-March and lasting through April (Fig. 4; Tables A3–A5). For cities where restrictions have been mainly removed (Wuhan, Milan) concentrations rise back towards the BCM value, although the concentrations in neither city have been fully re-
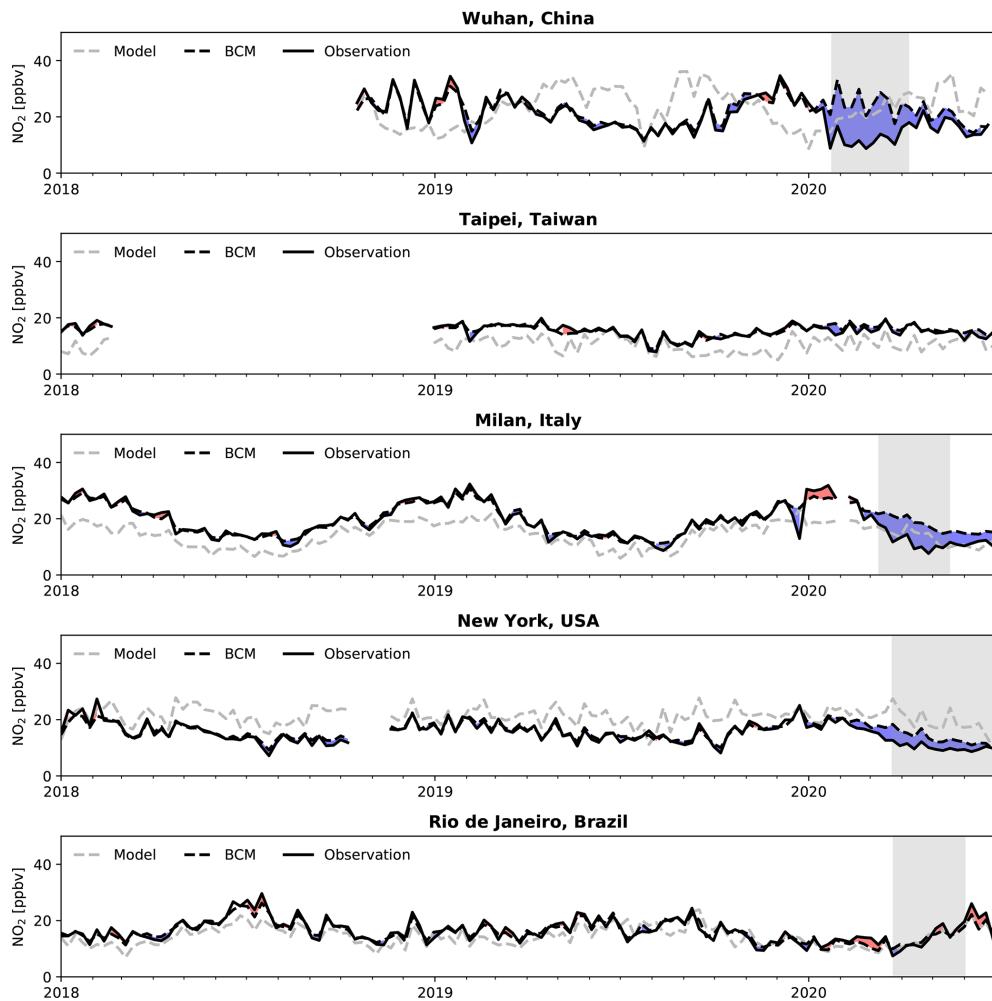
Figure 4. Comparison of NO_2 surface concentrations (ppbv = nmol mol^{-1}) for Wuhan, Taipei, Milan, New York, and Rio de Janeiro for January 2018 through June 2020. Observed values are shown in solid black, the original GEOS-CF model simulation is shown in dashed grey, and the BCM predictions are in dashed black. The area between observations and BCM predictions is shaded blue (red) if observations are lower (higher) than BCM predictions. Grey areas represent the period of lockdown. Shown are the 7 d average mean values for the 9, 18, 19, 14, and 2 observational sites in Wuhan, Taipei, Milan, New York, and Rio de Janeiro, respectively. Observations for China are only available starting in mid-September 2018.

stored to what might be expected based on the business-as-usual GEOS-CF simulation.

Looking more broadly at cities around the globe, 53 of the 64 specifically analyzed cities feature NO_2 reductions of between 20 %–50 % (Figs. A6–A8 and Tables A3–A5). Most locations issued social distancing recommendations prior to the legal lockdowns and observed NO_2 declines often precede the official lockdown date by 7–14 d (e.g., Brussels, London, Boston, Phoenix, and Washington, D.C.).

For Taipei and Rio de Janeiro, the observations and the BCM show little difference (Fig. 4), consistent with the less stringent quarantine measures in these places. Other cities with only short-term NO_2 reductions of less than 25 % include Atlanta (USA), Prague (Czech Republic), and Melbourne (Australia), again fitting with the comparatively re-laxed containment measures in these places (Figs. A6–A8). In contrast, Tokyo (Japan) and Stockholm (Sweden), which also implemented a less aggressive COVID-19 response, exhibit NO_2 reductions comparable to those of cities with official lockdowns (>20 %), suggesting that economic and human activities were similarly subdued in those cities.

Substantial differences exist between cities in South America, with Rio de Janeiro and Santiago de Chile showing little change over the analyzed period, whereas Quito (Ecuador) and Medellín (Colombia) experienced a greater than 50 % reduction in NO_2 after the initiation of strict restrictions measures in mid-March (Fig. A8 and Table A5). Concentrations in Medellín rebounded sharply in April and May, while concentrations in Quito remained 55 (52–58) %

below business as usual throughout May and only started to return back to normal in June.

To evaluate the large-scale impact of COVID-19 restrictions on air quality, we aggregate the individual observation–model comparisons by country. We note that our estimates for some countries (e.g., Brazil, Colombia) are based on a single city and likely not representative of the whole country. On a country level, we find the sharpest and earliest drop in NO_2 over China, where observed concentrations fell, on average, 55 (51–59) % below their expected value in early February when restrictions were implemented (Fig. 5). Concentrations remained at this level until late February, at which point they started to increase until restrictions were significantly relaxed in early April. Our analysis suggests that Chinese NO_2 concentrations have recovered to within 5 (1–9) % of the business-as-usual values since then. For 2019 (dashed line in Fig. 5) the BCM shows a reduction in NO_2 concentrations around Chinese New Year (5 February 2019), and it is likely that some reduction around the equivalent 2020 period (25 January 2020) would have occurred anyway. However, the 2020 reductions are significantly larger and more prolonged than in 2019. Similar to China, India shows large reductions in NO_2 concentration (58 (49–67) %) coinciding with the implementation of restrictions in mid-March (Fig. 5); however, NO_2 concentrations have not yet recovered by the end of June, reflecting the prolonged duration of lockdown measures. Other areas of Asia, such as Hong Kong and Taipei, implemented smaller restrictions than China or India and they show significantly smaller decreases (less than 20 %).

For Europe and the United States, we find widespread NO_2 reductions averaging 22 (19–25) % in March and 33 (30–36) % in April (Fig. 5). In some countries, recovery is evident as lockdown restrictions are removed or lessened (e.g., Greece, Romania), but in 29 out of 36 countries concentrations remain 20 % or more below the business-as-usual scenario throughout May and June.

3.2   Ozone

We follow the same methods for developing a business-as-usual counterfactual for O_3 as we did for NO_2 in Sect. 3.1. Any change in local O_3 concentration arising from COVID-19 restrictions is set against a large seasonal increase in (background) concentrations in the Northern Hemisphere springtime (Fig. 6). Due to the longer atmospheric lifetime of O_3 compared to NO_2, the local O_3 signal is expected to be comparatively small. This makes attributing changes in O_3 concentration more challenging than for NO_2. Our analysis shows an O_3 increase of up to 50 % for some periods in cities with large NO_2 reductions (e.g., Wuhan, Milan, Quito; Figs. 3 and A9–A11), but there is much less convincing evidence for a systematic O_3 response across cities or on a regional level (Fig. 7). For example, our analysis shows little O_3 difference in Beijing and Madrid during lockdown despite

NO_2 declines comparable to Wuhan or Milan (Figs. A9–A11). O_3 enhancements of up to 20 % are found over Europe (e.g., Belgium, Luxembourg, Serbia), with a peak in early April, approximately 2 weeks after lockdown started (Fig. 7).

The analysis of O_3 is complicated by its nonlinear chemical response to NO_x emissions. In the presence of sunlight, O_3 is produced chemically from the oxidation of volatile organic compounds in the presence of NO_x (Seinfeld and Pandis, 2016). Therefore, a decline in NO_x emissions could decrease O_3 production and thus suppress O_3 concentrations. On the other hand, the process of NO_x titration, in which freshly emitted NO rapidly reacts with O_3 to form NO_2, acts as a sink for O_3 (Seinfeld and Pandis, 2016). Odd oxygen (O_x) is conserved when O_3 reacts with NO and thus offers a tool for separating these competing processes. Figure 8 presents the global mean diurnal cycle for O_3 and O_x for the 5-month period since 1 February 2020 for both the observations and the BCM model, based on the individual hourly predictions at each observation site aggregated by local hour. The analysis of O_3 and O_x is based on the same set of observation sites where both NO_2 and O_3 observations are available (see Fig. 1). Compared to the BCM model, there has been an increase in the concentration of nighttime O_3 (00:00–05:00 LT, local time, Fig. 8a) by 1 ppbv ($ppbv = nmol \, mol^{-1}$) compared to the BCM, whereas O_x shows a decrease of 1 ppbv (Fig. 8b). While these changes are small in magnitude, they represent a multi-month aggregate over 3485 observation sites that are statistically significant at the 1 % confidence interval. It should be noted that the biases of the machine learning models show little diurnal variability (Figs. A12–13), suggesting that this result is not caused by poor model performance during specific times of the day.

Our results indicate that during the night reduced NO emissions led to a reduction in O_3 titration, allowing O_3 concentrations to increase. During the afternoon, we find that O_3 concentrations are lower by 1 ppbv (Fig. 8a), while observed O_x concentrations are lower than the baseline model by almost 2 ppbv at 14:00 LT (Fig. 8b). We attribute the lower O_x to reduced net O_x production due to the lower NO_x concentration, but as titration is also reduced, daytime O_3 concentrations change little. Overall changes to mean O_3 concentrations are small, but there is a flattening of the diurnal cycle.

As shown in the lower panels in Fig. 8, both factors – enhanced nighttime O_3 and reduced daytime O_x – are more pronounced at locations where preexisting NO_2 concentrations are high (>15 ppbv). This suggests that the observed O_3 deviations from the BCM are indeed coupled to NO_x reductions due to COVID-19 restrictions, given that those are most pronounced at polluted sites.

3.3 NO_x emission reductions

The NO_2 analysis presented in Sect. 3.1 implies a stark reduction in NO_x emissions. However, due to the impact of
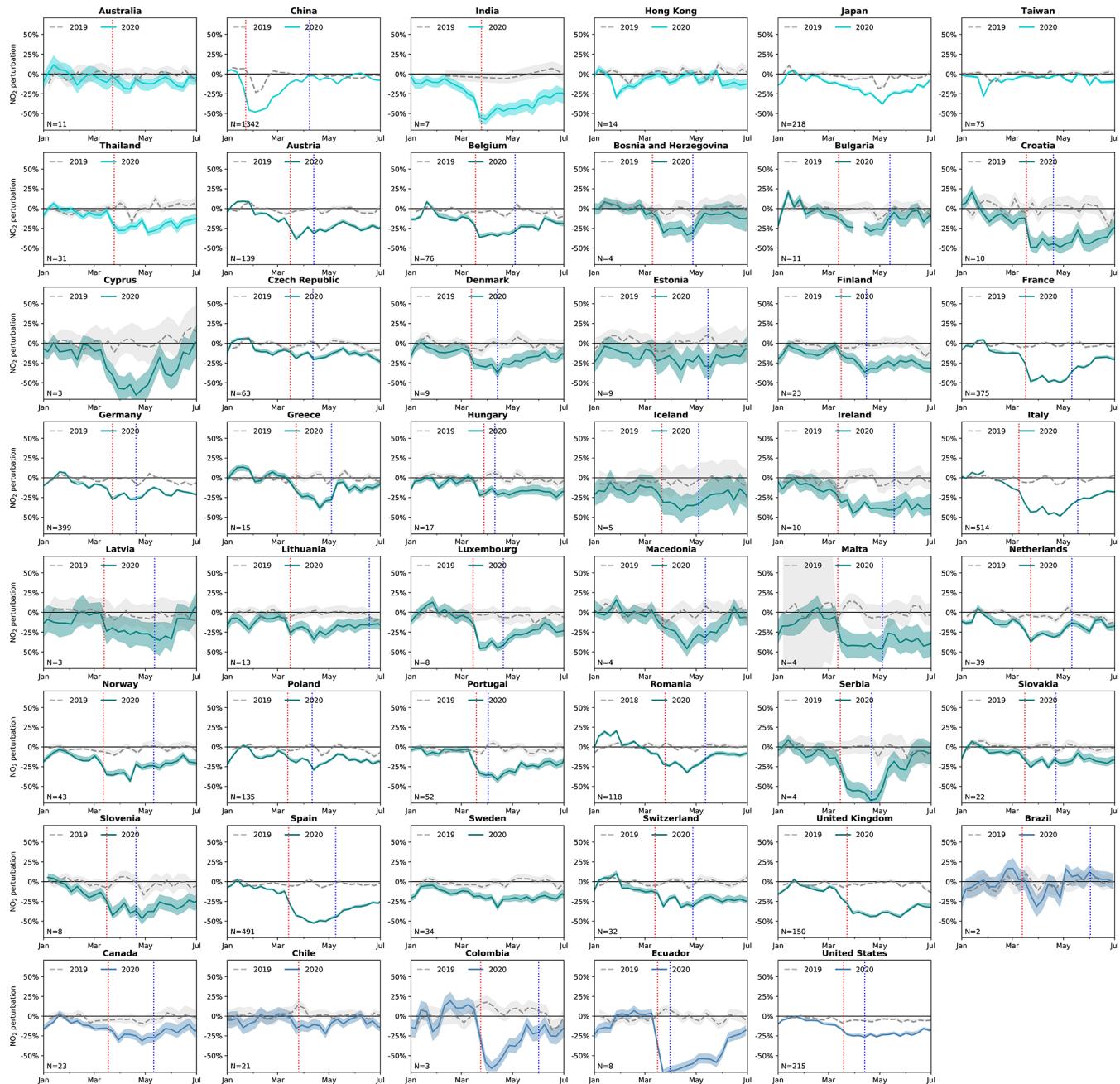
Figure 5. The 7 d average fractional difference between observed NO_2 and the BCM predictions for 46 countries between 1 January through 30 June, aggregated from all sites across each country (number of sites given at the bottom left of each panel). The thick line indicates the mean across all sites for the first half of 2020, with the shaded area representing the uncertainty estimate. Differing colors indicate differing regions (cyan: Asia and Australia; green: Europe; blue: Americas). The dashed grey line indicates the equivalent average for the same 6 month period in 2019 (note that 2019 data was included in the training). The dashed vertical red line indicates COVID-19 restriction dates, and the blue line indicates the beginning of easing measures.

atmospheric chemistry, changes in NO_2 concentrations do not reflect the same relative change in NO_x emissions. Because of this, the NO_2 / NO_x ratio and the NO_x lifetime, both of which depend on seasonality and the local chemical environment, need to be taken into account when infer-

ring NO_x emissions from NO_2 concentrations (Lamsal et al., 2011; Shah et al., 2020). To estimate the relationship between changes in NO_x emission and changes in NO_2 concentrations, we conducted a sensitivity simulation for the time period 1 December 2019 to 8 June 2020 using the
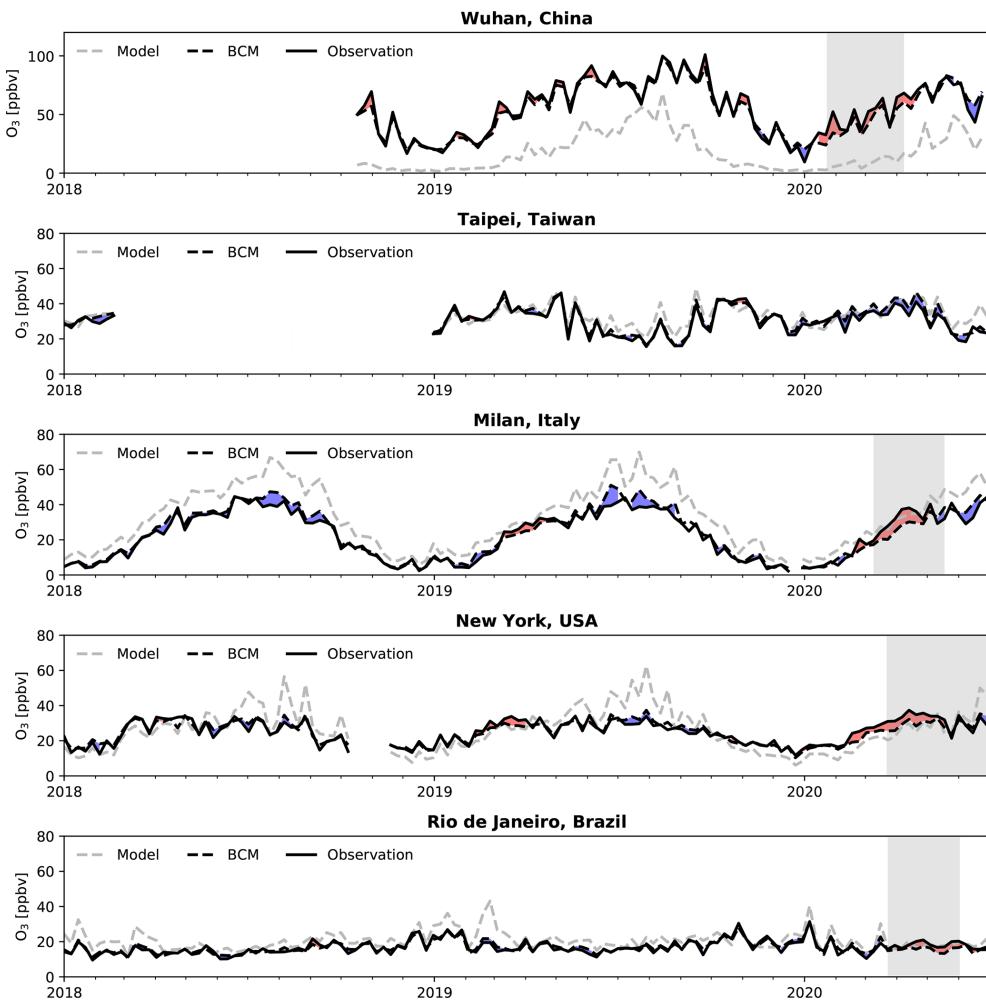
Figure 6. Comparison of O_3 surface concentrations for Wuhan, Taipei, Milan, New York, and Rio de Janeiro for January 2018 through June 2020. Observed values are shown in solid black, the original GEOS-CF model simulation is shown in dashed grey, and the BCM predictions are in dashed black. The area between observations and BCM predictions is shaded blue (red) if observations are lower (higher) than BCM predictions. The grey areas represent the period of lockdown. Shown are the 7 d average mean values for the 9, 18, 19, 14, and 4 observational sites in Wuhan, Taipei, Milan, New York, and Rio de Janeiro, respectively. Observations for China are only available starting in mid-September 2018.

GEOS-CF model with perturbed anthropogenic emissions. The perturbation simulation uses anthropogenic NO_x emissions scaled based on adjustment factors derived from NO_2 tropospheric columns observed by the NASA OMI instrument (Boersma et al., 2011). Daily scale factors were computed by normalizing coarse-resolution ($2 \times 2.5°$) 14 d NO_2 tropospheric column moving averages by the corresponding moving average for year 2018 (the emissions base year in GEOS-CF; Sect. 2.2). Forest fire signals were filtered out based on QFED emissions and no scaling was applied over water. This results in anthropogenic emission adjustment factors of 0.3 to 1.4 (Fig. A14), comparable to the magnitude obtained from the observation–BCM comparisons at cities globally (Fig. 5) and capturing the range of expected NO_x emission changes. However, it should be noted that the scale

factors do not necessarily coincide in space and time with the ones derived from observations and the BCM, and they do not include any adjustment for the NO_2 / NO_x ratio.

Figure 9a shows the response of NO_2 surface concentration to a change in NO_x emissions derived from the comparison of the sensitivity experiment against the GEOS-CF reference simulation. Our results indicate that NO_2 concentrations drop, on average, by 80 % of the fractional decrease in anthropogenic NO_x emission, with a further diminishing effect for emission reductions greater than 50 %. This reflects both the buffering effect of atmospheric chemistry and the presence of natural background NO_2. The here-derived average sensitivity of 0.8 between a change in surface NO_2 to a change in NO_x emissions is comparable to the value of 0.86 (1/1.16) obtained by Lamsal et al. (2011) for the relation-
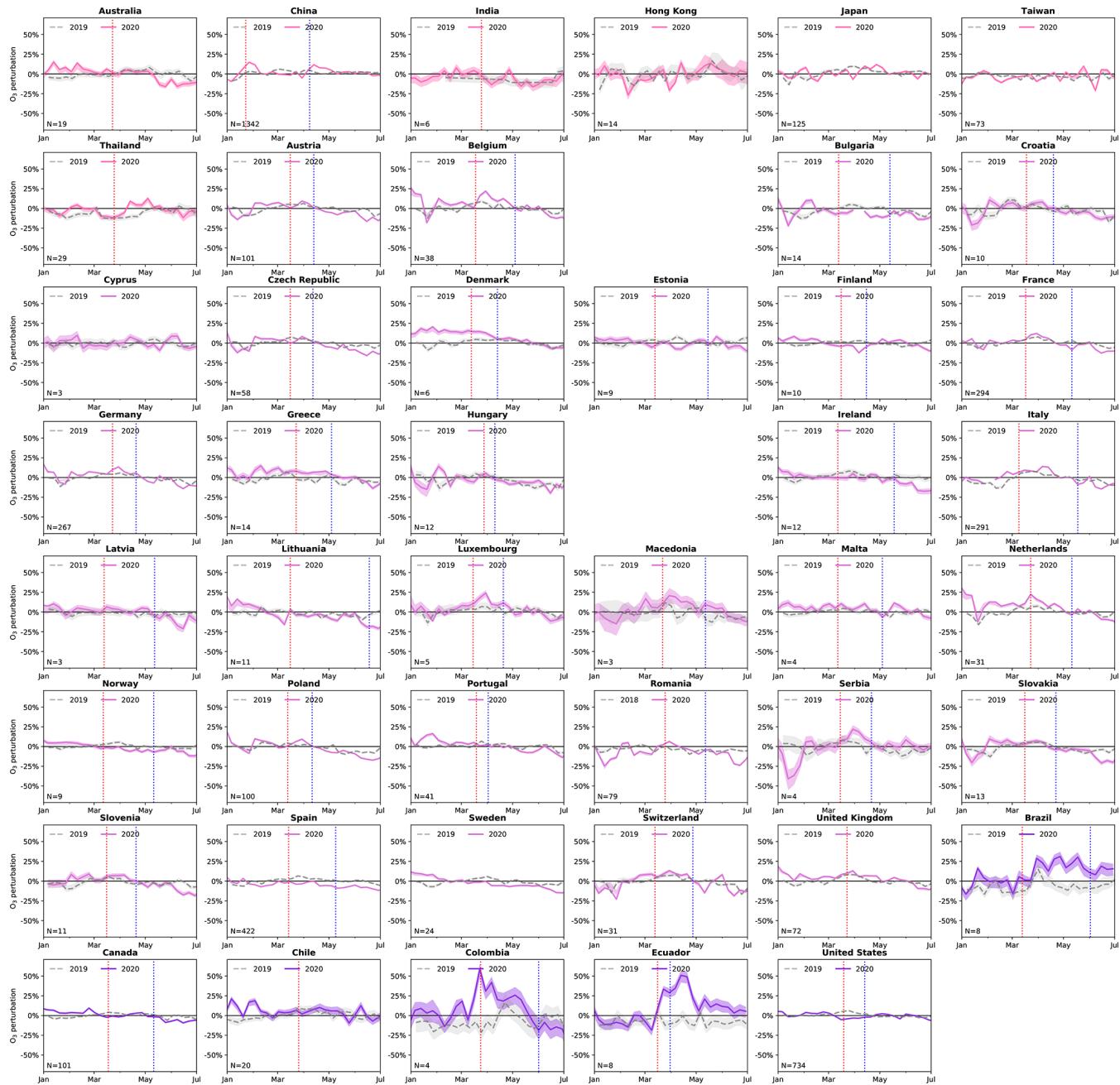
Figure 7. Similar to Fig. 5 but for O_3 and without Bosnia and Herzegovina and Iceland. Differing colors indicate differing regions (pink: Asia and Australia; light purple: Europe; dark purple: Americas).

ship between NO_x emissions and tropospheric column NO_2 observations.

To infer the reduction in anthropogenic NO_x emissions due to COVID-19 containment measures during the first 6 months of 2020, we use the best linear fit between the simulated NO_x / NO_2 sensitivity (dashed purple line in Fig. 9a). To do so, we calculate the monthly percentage emission change at each observation site based on the NO_2 anomalies derived in Sect. 3.1 and the corresponding best fit NO_x / NO_2

sensitivity (Fig. 9a). This is a simplification, as the local NO_x / NO_2 sensitivity ratio is highly dependent on the local environment. To account for this uncertainty, we assign an absolute error of 15 % to our NO_x / NO_2 sensitivity, as derived from the spread in the NO_x / NO_2 ratio in the sensitivity simulation (Fig. 9a). We then aggregate these estimates to a country level by weighting them based on average NO_2 concentrations per location, thus giving higher weight to locations with more nearby NO_x emission sources. It should be
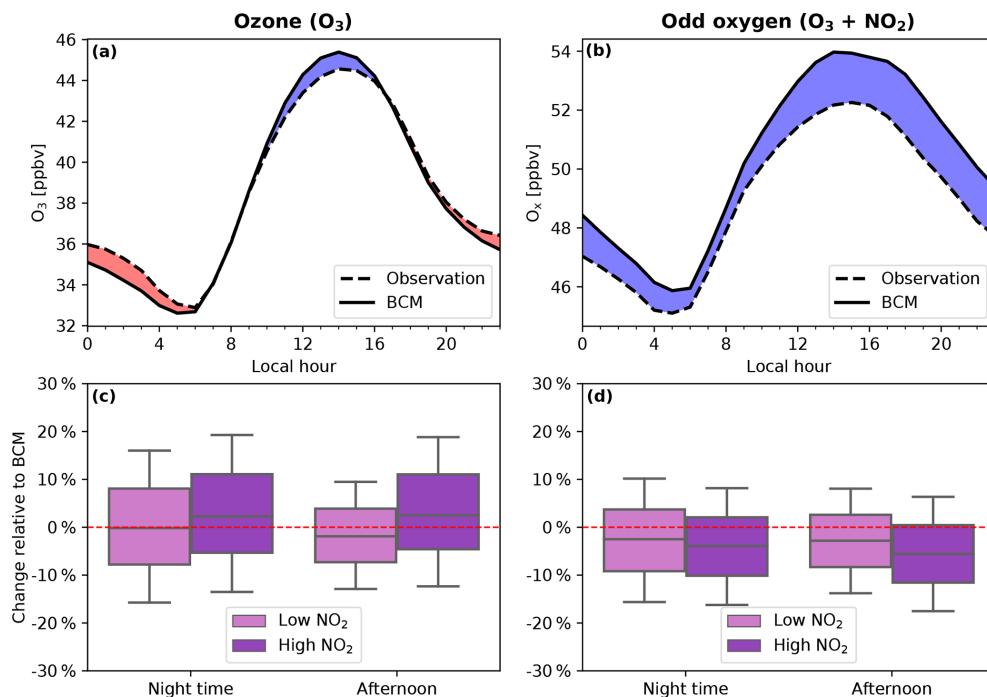
Figure 8. Observed and BCM-modeled diurnal cycle of O_3 **(a)** and O_x **(b)** averaged across all surface observation sites between 1 February 2020 through 30 June 2020 with estimated corresponding changes in surface O_3 **(c)** and O_x **(d)** relative to the BCM. Bar plots (**c** and **d**) show observed changes during nighttime (0:00–05:00 LT) and the afternoon (12:00–17:00 LT) for locations with low (<15 ppbv) and high (>15 ppbv) NO_2 concentrations (based on the 2019 average).

noted that for some countries our estimates are based upon a small number of observation sites that might not be representative for the country as a whole. This is particularly true for India and Brazil, where less than 10 observation sites are available. While the smaller observation sample size is reflected in the wider uncertainty associated with these emission estimates compared to countries with a much denser monitoring network (e.g., China or Europe), the applied extrapolation method might incur errors that are not reflected in the stated uncertainty ranges.

To obtain absolute estimates in emission changes, the monthly country-level percentage emission changes are convoluted with bottom-up emissions estimates for 2015 from the Emission Database for Global Atmospheric Research (EDGAR v5.0_AP; Crippa et al., 2018, 2020). The choice of EDGAR v5.0 as the bottom-up reference inventory (over, e.g., the HTAP emissions inventory used in GEOS-CF) was motivated by the fact that its baseline has been updated more recently and the country emission totals – which our analysis is based on – are readily available.

As summarized in Table 2, we calculate that the total reduction in anthropogenic NO_x emissions due to COVID-19 containment measures during the first 6 months of 2020 amounted to 3.1 (2.6–3.6) TgN (Fig. 9b and Table 2). This is equivalent to 5.5 (4.7–6.4) % of global annual anthropogenic NO_x emissions (Table 2). Our estimate encompasses 46 countries that together account for 67 % of the total emis-

sions (excluding international shipping and aviation). We have no information for significant countries such as Russia, Indonesia, or anywhere in Africa due to the lack of publicly available near-real-time air quality information. China accounts for the largest fraction of the total deduced emission reductions (28 %), followed by India (25 %), the United States (18 %), and Europe (12 %).

While our method does not allow for sector-specific emission attribution, we assume our results to be most representative for changes in traffic emissions (rather than say aircraft emissions) given the location of the observation sites. On average, traffic emissions represent 27 % of total anthropogenic NO_x emissions (Crippa et al., 2018), and our derived total NO_x emission reduction from January–June 2020 corresponds to 21 (17–24) % of global annual traffic emissions. The share of transportation on total NO_x emissions is higher in the US and Europe (approx. 40 %) compared to India and China (20 %–25 %). Taking this into account, the derived ratio of NO_x emission reductions to annual traffic emissions is 21 (16–26) % in the US, 25 (20–30) % in Europe, 39 (34–44) % in China, and 62 (55–69) % in India.

3.4 Long-term impact of reduced NO_x emissions on surface O_3

The response of O_3 to NO_2 declines in the wake of the COVID-19 outbreak is complicated by the competing in-
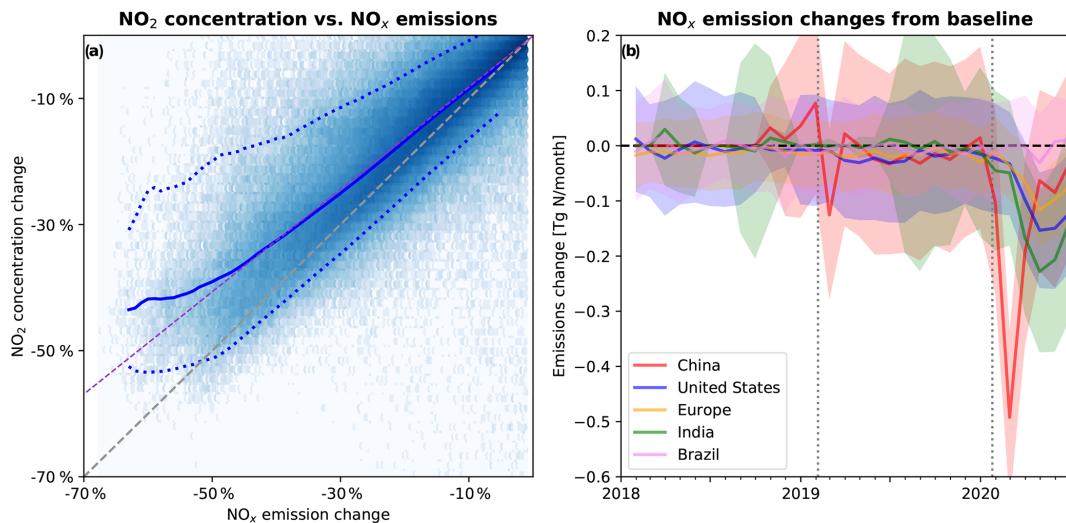
Figure 9. (a) Response of NO_2 surface concentration (*y* axis) to a change in NO_x emissions (*x* axis), as deduced from a model sensitivity simulation (see methods). The solid blue line shows the mean value across all individual grid cells (blue squares) and the dotted blue lines show the 5 % and 95 % quantiles. The dashed purple line shows the best linear fit. **(b)** Estimated monthly change in NO_x emissions from the baseline since 2018 for China (red), the United States (blue), Europe (yellow), India (green), and Brazil (purple), as estimated from observed NO_2 concentration anomalies. Shaded areas indicate estimated emission uncertainties. Dotted grey lines indicate Chinese New Year 2019 and 2020.

fluences of atmospheric chemistry. From February through June 2020, the diurnal observation-BCM comparisons suggest that the reduction in photochemical production was offset by a smaller loss from titration, as described in Sect. 3.2. This resulted in a flattening of the diurnal cycle and an insignificant net change in surface O_3 over a diurnal cycle. The competing impacts of reduced NO_x emissions on O_3 production and loss are dependent on the local chemical and meteorological environment. This is reflected in the variable geographical response of O_3 following the implementation of COVID-19 restrictions (Le et al., 2020; Dantas et al., 2020). Moreover, as atmospheric reactivity increases through the Northern Hemisphere spring and summer, the relative importance of photochemical production is expected to increase in the Northern Hemisphere.

To assess the potential seasonal-scale impact of reduced anthropogenic emissions on O_3, we conducted two free-running forecast simulations between 8 June and 31 August 2020, initialized from the GEOS-CF simulation and the sensitivity simulation described in Sect. 3.3, respectively. Both simulations use the same biomass burning emissions based on a historical QFED climatology. For the forecast sensitivity experiment, we assume a sustained, time-invariant 20 % reduction in global anthropogenic emissions of NO_x, carbon monoxide (CO), and VOCs. We chose to alter not only the anthropogenic emissions of NO_x but also other pollutants whose anthropogenic emissions are highly correlated to NO_x, as a reduction in NO_x emissions without corresponding declines in CO and VOC emissions seems unrealistic.

Figure 10 shows the differences between the reference forecast and the sensitivity simulation over the United States, Europe, and China. Our results indicate that sustained lower anthropogenic emissions lead to a general decrease in surface O_3 concentrations of 10 %–20 % over eastern China, Europe, and the western and northeastern US during July and August relative to the business-as-usual reference forecast simulation. However, it is also notable that in some locations the model forecast O_3 concentrations increase by an equivalent amount (e.g., Scandinavia, southern central US and Mexico, northern India), reflecting the high nonlinearity of atmospheric chemistry. This highlights the complex interactions between emissions, chemistry, and meteorology and their impact on air pollution on different time scales.

4   Conclusions

The combined interpretation of observations and model simulations using machine learning can be used to remove the confounding effect of meteorology and atmospheric chemistry, offering an effective tool to monitor and quantify changes in air pollution in near-real time. The global response to the COVID-19 pandemic presents a perfect test bed for this type of analysis, offering insights into the interconnectedness of human activity and air pollution. While national mitigation strategies have led to substantial regional NO_2 concentration decreases over the past decades in many places (e.g., Hilboll et al., 2013; Russell et al., 2012; Castellanos and Boersma, 2012), the widespread and near-instantaneous reduction in NO_2 following the imple-

Table 2. Anthropogenic NO_x emission reductions in GgN month^{-1} as derived from NO_2 concentration changes.

	Baseline[a]	Feb 2020	Mar 2020	Apr 2020	May 2020	Jun 2020
Australia	621	−2.9 (−13.8–8.0)	−3.7 (−14.4–6.9)	−8.5 (−18.5–1.6)	−6.1 (−16.1–3.8)	−7.9 (−17.6–1.8)
Austria	73	−0.5 (−1.4–0.5)	−1.7 (−2.7−−0.7)	−2.0 (−3.0−−1.0)	−1.6 (−2.6−−0.6)	−1.8 (−2.8−−0.8)
Belgium	98	−1.0 (−2.4−0.3)	−2.0 (−3.4−−0.7)	−3.2 (−4.5−−1.9)	−2.4 (−3.8−−1.1)	−1.8 (−3.2−−0.5)
Bosnia and Herzegovina	32	0.05 (−0.47–0.57)	−0.43 (−0.96–0.11)	−0.90 (−1.45−−0.35)	−0.39 (−0.99–0.21)	−0.28 (−0.92–0.35)
Brazil	1844	−1.3 (−35.7–33.2)	−1.5 (−37.0–34.0)	−32.0 (−67.2–3.2)	7.2 (−26.1–40.6)	10.3 (−21.7–42.3)
Bulgaria	46	−0.12 (−0.83–0.58)	−0.60 (−1.32–0.12)	−1.20 (−1.93−−0.46)	−0.67 (−1.44–0.11)	−0.41 (−1.20–0.37)
Canada	755	−6.3 (−17.1–4.6)	−12.2 (−23.3−−1.1)	−19.8 (−31.4−−8.1)	−18.5 (−30.5−−6.5)	−11.4 (−23.8−1.0)
Chile	202	−0.5 (−3.9–2.9)	−0.7 (−4.0–2.6)	−2.8 (−6.0–0.4)	−1.6 (−4.7–1.4)	−1.0 (−4.1–2.1)
China	11876	−517 (−669−−366)	−191 (−342−−39)	−63 (−215−89)	−82 (−235−70)	−30 (−182−123)
Colombia	207	1.2 (−2.5–4.9)	−0.2 (−3.8–3.4)	−12.0 (−15.5−−8.5)	−5.5 (−9.1−−1.9)	−4.4 (−8.0−−0.7)
Croatia	24	−0.25 (−0.64−0.14)	−0.55 (−0.95−−0.15)	−1.03 (−1.44−−0.63)	−0.96 (−1.37−−0.55)	−0.90 (−1.31−−0.48)
Czech Republic	108	−1.0 (−2.5–0.4)	−1.3 (−2.8–0.2)	−1.8 (−3.2−−0.3)	−1.3 (−2.8–0.2)	−1.6 (−3.1−−0.1)
Denmark	48	−0.5 (−1.3–0.3)	−0.8 (−1.6−−0.1)	−1.4 (−2.1−−0.6)	−1.0 (−1.8−−0.2)	−0.8 (−1.5−−0.0)
Ecuador	133	0.5 (−1.6–2.6)	−3.8 (−5.9−−1.8)	−8.9 (−11.0−−6.9)	−7.5 (−9.6−−5.4)	−4.0 (−6.1−−2.0)
Estonia	13	−0.20 (−0.44−0.05)	−0.16 (−0.41−0.10)	−0.28 (−0.54−−0.02)	−0.29 (−0.54−−0.03)	−0.20 (−0.45−−0.04)
Finland	77	−1.1 (−2.3−0.1)	−0.8 (−2.0−0.4)	−2.3 (−3.6−−1.1)	−2.0 (−3.3−−0.8)	−2.0 (−3.3−−0.8)
France	337	−3.2 (−7.6−1.2)	−9.1 (−13.5−−4.7)	−15.7 (−20.1−−11.3)	−12.7 (−17.1−−8.2)	−6.9 (−11.3−−2.4)
Germany	494	−3.0 (−9.4–3.4)	−7.1 (−13.5−−0.7)	−11.5 (−17.9−−5.1)	−8.3 (−14.7−−1.9)	−9.2 (−15.7−−2.8)
Greece	101	0.1 (−1.4–1.5)	−0.5 (−1.9−1.0)	−2.9 (−4.4−−1.5)	−1.5 (−3.0−−0.0)	−1.3 (−2.8−−0.1)
Hong Kong, China	90	−1.5 (−2.8−−0.2)	−0.2 (−1.6−1.1)	−0.4 (−1.7−1.0)	−0.3 (−1.6−1.0)	−1.2 (−2.6−0.2)
Hungary	55	−0.3 (−1.1–0.5)	−0.4 (−1.2−0.4)	−1.0 (−1.8−−0.2)	−1.0 (−1.8−−0.1)	−1.0 (−1.9−−0.2)
Iceland	2	−0.04 (−0.08−0.01)	−0.04 (−0.09−0.01)	−0.09 (−0.14−−0.04)	−0.07 (−0.12−−0.01)	−0.04 (−0.10−−0.01)
India	4693	−52 (−125−21)	−161 (−234−−88)	−232 (−307−−157)	−202 (−280−−125)	−140 (−220−−59)
Ireland	35	−0.3 (−1.0−0.3)	−0.8 (−1.4−−0.2)	−1.3 (−1.9−−0.7)	−1.4 (−2.0−−0.8)	−1.2 (−1.8−−0.6)
Italy	357	−1.9 (−6.5−2.7)	−9.7 (−14.4−−5.1)	−15.6 (−20.2−−10.9)	−12.4 (−17.1−−7.8)	−7.7 (−12.3−−3.0)
Japan	996	−4.1 (−17.2−9.0)	−12.6 (−25.7−0.6)	−23.4 (−36.7−−10.2)	−28.7 (−41.9−−15.4)	−18.0 (−31.3−−4.7)
Latvia	14	−0.08 (−0.38−0.22)	−0.16 (−0.45−0.12)	−0.37 (−0.67−−0.06)	−0.44 (−0.74−−0.13)	−0.18 (−0.48−0.12)
Luxembourg	12	−0.17 (−0.48−0.15)	−0.27 (−0.58−0.05)	−0.50 (−0.82−−0.18)	−0.40 (−0.72−−0.07)	−0.32 (−0.64−−0.01)
Lithuania	20	0.01 (−0.18−0.19)	−0.23 (−0.42−−0.05)	−0.47 (−0.65−−0.29)	−0.31 (−0.49−−0.13)	−0.23 (−0.42−−0.05)
North Macedonia	10	−0.00 (−0.17−0.16)	−0.08 (−0.25−0.09)	−0.33 (−0.50−−0.16)	−0.28 (−0.46−−0.10)	−0.06 (−0.24−−0.12)
Malta	3	−0.00 (−0.06−0.06)	−0.07 (−0.13−−0.01)	−0.13 (−0.20−−0.07)	−0.11 (−0.18−−0.05)	−0.11 (−0.18−−0.05)
Netherlands	121	−1.4 (−3.1−0.4)	−2.6 (−4.3−−0.8)	−3.4 (−5.1−−1.7)	−2.1 (−3.9−−0.4)	−2.0 (−3.8−−0.2)
Norway	63	−0.8 (−1.7−0.0)	−1.5 (−2.4−−0.6)	−1.9 (−2.8−−1.0)	−1.5 (−2.5−−0.6)	−1.1 (−2.0−−0.2)
Poland	284	−3.3 (−7.1−0.5)	−3.2 (−7.0−0.5)	−5.9 (−9.7−−2.1)	−4.0 (−7.8−−0.2)	−5.1 (−9.0−−1.3)
Portugal	70	−0.4 (−1.4−0.6)	−1.2 (−2.2−−0.2)	−2.6 (−3.6−−1.5)	−1.9 (−2.9−−0.9)	−1.6 (−2.6−−0.5)
Romania	102	0.5 (−0.9−1.8)	−1.1 (−2.5−0.3)	−2.5 (−3.9−−1.2)	−1.6 (−3.0−−0.2)	−1.0 (−2.4−0.4)
Serbia	63	−0.48 (−1.54−0.59)	−1.77 (−2.87−−0.68)	−3.83 (−4.94−−2.72)	−2.24 (−3.44−−1.04)	−0.82 (−2.07−0.43)
Slovakia	33	−0.20 (−0.67−0.28)	−0.43 (−0.90−0.05)	−0.61 (−1.09−−0.13)	−0.54 (−1.04−−0.05)	−0.57 (−1.07−−0.07)
Spain	333	−2.9 (−7.2−1.5)	−8.6 (−13.0−−4.2)	−17.0 (−21.3−−12.6)	−13.9 (−18.3−−9.5)	−10.0 (−14.5−−5.6)
Sweden	85	−1.0 (−2.2−0.2)	−1.3 (−2.5−−0.0)	−2.0 (−3.3−−0.8)	−1.9 (−3.1−−0.6)	−1.6 (−2.9−−0.4)
Switzerland	36	−0.25 (−0.77−0.26)	−0.65 (−1.16−−0.14)	−0.94 (−1.45−−0.43)	−0.83 (−1.36−−0.30)	−0.84 (−1.37−−0.31)
Taiwan	371	−3.7 (−8.6−1.2)	−1.5 (−6.4−3.5)	−1.3 (−6.2−3.7)	−1.7 (−6.7−3.4)	−3.9 (−8.9−1.2)
Thailand	458	−2.6 (−9.2−4.0)	−4.8 (−11.7−2.0)	−10.7 (−17.6−−3.8)	−11.6 (−18.6−−4.7)	−8.5 (−15.6−−1.4)
United Kingdom	390	−3.0 (−8.3−2.2)	−6.8 (−12.0−−1.6)	−16.4 (−21.6−−11.2)	−16.4 (−21.6−−11.1)	−12.8 (−18.0−−7.5)
United States	6243	−34 (−116−48)	−94 (−177−−11)	−155 (−239−−72)	−147 (−231−−64)	−123 (−207−−40)
Other countries[b]	1307	NA	NA	NA	NA	NA
Shipping and aviation	671	NA	NA	NA	NA	NA
Total	4681	−651 (−843−−460)	−553 (−745−−360)	−692 (−885−−498)	−603 (−798−−408)	−418 (−615−−222)

[a] EDGAR v5.0_AP 2015 annual emissions expressed as GgN month^{-1} (Crippa et al., 2020). [b] Primarily Indonesia, Iran, Mexico, Pakistan, Russia, Saudi Arabia, South Africa, South Korea, and Vietnam. NA: not available.

mentation of COVID-19 containment measures indicates that there is still large potential to lower human exposure to NO_2 through reduction of anthropogenic NO_x emissions.

The here-derived NO_2 reductions are in good agreement with other emerging estimates. For instance, we determine an 18 % decline over China for the 20 d after Chinese New Year relative to the preceding 20 d, consistent with the 21 % reduction reported in Liu et al. (2020a). Similarly, our estimated 22 % reduction over China for January to March 2020 is in excellent agreement with the 21 %–23 % reported by Liu et al. (2020b). For Spain, we obtain an NO_2 reduction of 46 % between March 14 to 23 April , again in close agreement with the values reported in Petetin et al. (2020).

While large reductions in NO_2 concentrations are achievable and immediately follow curtailments in NO_x emissions, the O_3 response is more complicated and can be in the opposite direction, at times by as much as 50 % (Jhun et al., 2015; Le et al., 2020). The O_3 response is dependent on season, timescale, and environment, with an overall tendency to lower surface O_3 under a scenario of sustained NO_x emission reductions. This shows the complexities faced by policy makers in curbing O_3 pollution.
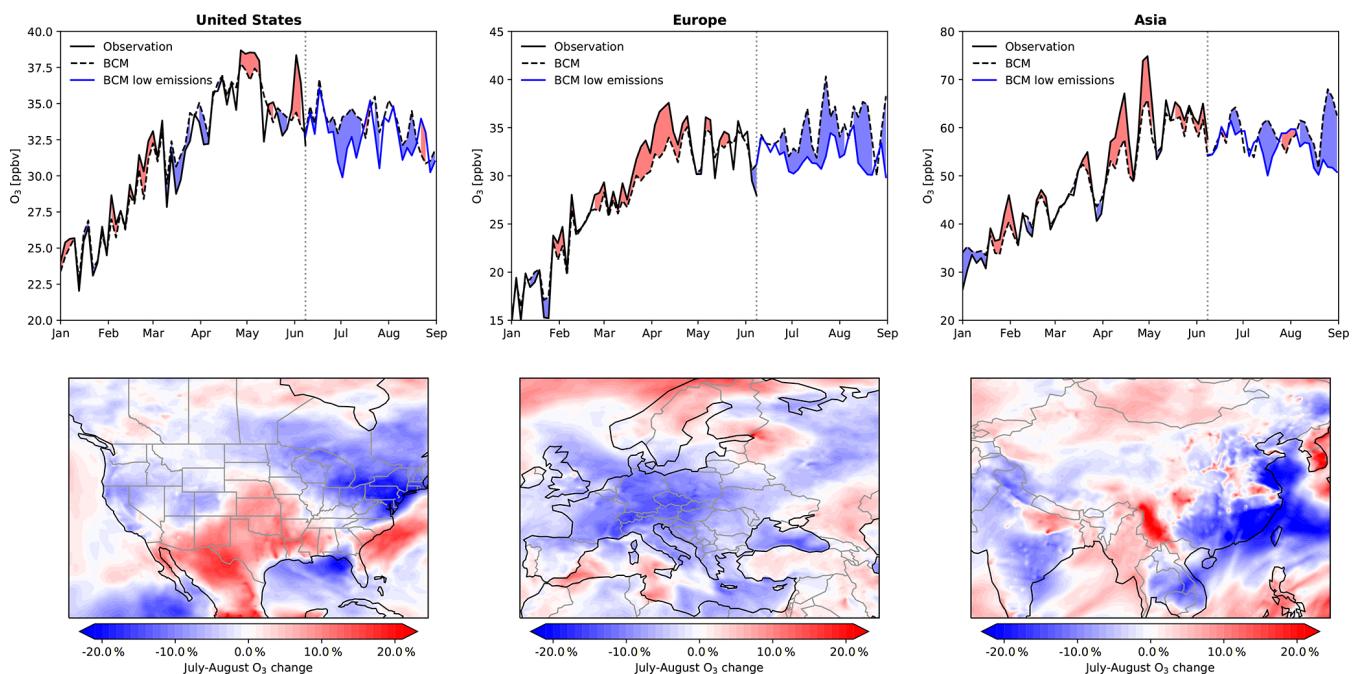
Figure 10. Change in mean surface O_3 over the United States, Europe, and Asia for a sensitivity simulation with altered anthropogenic emissions. The top panels show daily average O_3 concentrations at all observation sites within the given region (solid black, January–June), the bias-corrected GEOS-CF model ("BCM", solid black, 1 January–8 June) continued with a business-as-usual GEOS-CF forecast from 9 June to 31 August, and GEOS-CF forecast assuming sustained 20 % anthropogenic emission reduction (blue). The bottom panels show mean changes in surface O_3 for July and August for the low emissions simulation relative to the business-as-usual forecast.

Appendix A

Table A1. List of input features fed into the XGBoost machine learning model.

Short name	Description	Unit
no2	nitrogen dioxide	ppbv
no	nitrogen oxide	ppbv
noy	reactive nitrogen (no + no2 + nitrates)	ppbv
o3	ozone	ppbv
co	carbon monoxide	ppbv
acet	acetone	ppbv
alk4	alkanes	ppbv
ald2	acetaldehyde	ppbv
hcho	formaldehyde	ppbv
c2h6	ethane	ppbv
c3h8	propane	ppbv
bcpi	hydrophilic black carbon	ppbv
bcpo	hydrophobic black carbon	ppbv
ocpi	hydrophilic organic carbon	ppbv
ocpo	hydrophobic organic carbon	ppbv
eoh	ethanol	ppbv
dst1	dust with diameter of $0.7\,\mu$	ppbv
dst2	dust with diameter of $1.4\,\mu$	ppbv
dst3	dust with diameter of $2.4\,\mu$	ppbv
dst4	dust with diameter of $4.5\,\mu$	ppbv
h2o2	hydrogen peroxide	ppbv
hno3	nitric acid	ppbv
hno4	peroxynitric acid	ppbv
isop	isoprene	ppbv
macr	methacrolein	ppbv
mek	methyl ethyl ketone	ppbv
mvk	methyl vinyl ketone	ppbv
n2o5	dinitrogen pentoxide	ppbv
nh3	ammonia	ppbv
nh4	ammonium	ppbv
nit	inorganic nitrates	ppbv
pan	peroxyacetyl nitrate	ppbv
prpe	alkenes	ppbv
rcho	aldehyde	ppbv
sala	fine sea salt aerosol	ppbv
salc	coarse sea salt aerosol	ppbv
so2	sulfur dioxide	ppbv
soap	secondary organic aerosol precursor	ppbv
soas	simple secondary organic aerosol	ppbv
tolu	toluene	ppbv
xyle	xylene	ppbv
ox	odd oxygen (o3 + no2)	ppbv
pm25_gcc	total $PM_{2.5}$	$\mu g\,m^{-3}$
pm25ni_gcc	nitrate $PM_{2.5}$	$\mu g\,m^{-3}$
pm25su_gcc	sulfate $PM_{2.5}$	$\mu g\,m^{-3}$
pm25ss_gcc	sea salt $PM_{2.5}$	$\mu g\,m^{-3}$
pm25du_gcc	dust $PM_{2.5}$	$\mu g\,m^{-3}$
pm25bc_gcc	black carbon $PM_{2.5}$	$\mu g\,m^{-3}$
pm25oc_gcc	organic carbon $PM_{2.5}$	$\mu g\,m^{-3}$
pm25soa_gcc	secondary organic aerosol $PM_{2.5}$	$\mu g\,m^{-3}$
pm25_gocart	total $PM_{2.5}$ as calculated by the GOCART model	$\mu g\,m^{-3}$

Table A1. Continued.

Short name	Description	Unit
hour	hour of day	–
weekday	day of the week	–
month	month of the year	–
trendday	days since 1 Jan 2018	d
cldtt	total cloud fraction	unitless
ps	surface pressure	Pa
q10m	specific humidity at 10 m	$kg\,kg^{-1}$
t10m	temperature at 10 m	K
tprec	total precipitation	mm
ts	skin surface temperature	K
u10m	10 m East-West wind-speed	$m\,s^{-1}$
v10m	10m North-South wind speed	$m\,s^{-1}$
zpbl	planetary boundary layer height	m
emis_no	nitrogen oxide emissions	$\mu g\,m^{-2}\,s^{-1}$
emis_co	carbon monoxide emissions	$\mu g\,m^{-2}\,s^{-1}$
emis_acet	acetone emissions	$\mu g\,m^{-2}\,s^{-1}$
emis_ald2	acetaldehyde emissions	$\mu g\,m^{-2}\,s^{-1}$
emis_alk4	alkanes emissions	$\mu g\,m^{-2}\,s^{-1}$
emis_benz	benzene emissions	$\mu g\,m^{-2}\,s^{-1}$
emis_c2h6	ethane emissions	$\mu g\,m^{-2}\,s^{-1}$
emis_prpe	alkenes emissions	$\mu g\,m^{-2}\,s^{-1}$
emis_tolu	toluene emissions	$\mu g\,m^{-2}\,s^{-1}$
emis_xyle	xylene emissions	$\mu g\,m^{-2}\,s^{-1}$
emis_isop	isoprene emissions	$\mu g\,m^{-2}\,s^{-1}$
emis_bcpi	hydrophilic black carbon emissions	$\mu g\,m^{-2}\,s^{-1}$
emis_bcpo	hydrophobic black carbon emissions	$\mu g\,m^{-2}\,s^{-1}$
emis_ocpi	hydrophilic organic carbon emissions	$\mu g\,m^{-2}\,s^{-1}$
emis_ocpo	hydrophobic organic carbon emissions	$\mu g\,m^{-2}\,s^{-1}$
emis_sala	fine sea salt aerosol emissions	$\mu g\,m^{-2}\,s^{-1}$
emis_salc	coarse sea salt aerosol emissions	$\mu g\,m^{-2}\,s^{-1}$
emis_so2	sulfur dioxide emissions	$\mu g\,m^{-2}\,s^{-1}$
emis_soap	secondary organic aerosol precursor emissions	$\mu g\,m^{-2}\,s^{-1}$
emis_soas	simple secondary organic aerosol emissions	$\mu g\,m^{-2}\,s^{-1}$
emis_chbr3	bromoform emissions	$\mu g\,m^{-2}\,s^{-1}$

Table A2. National lockdown dates used for visualizations.

Country	Start date	End date
Australia	23 March	–
Austria	16 March	13 April
Belgium	18 March	4 April
Bosnia and Herzegovina	10 March	27 April
Brazil	13 March	2 June
Bulgaria	13 March	13 May
Canada	18 March	11 May
Chile	26 March	–
China	23 Jan	8 April
Colombia	24 March	1 June
Croatia	18 March	19 April
Czech Republic	16 March	12 April
Denmark	13 March	13 April
Ecuador	16 March	31 March
Estonia	13 March	15 May
Finland	16 March	15 April
France	17 March	11 May
Germany	23 March	20 April
Greece	23 March	4 May
Hungary	28 March	10 April
Iceland	21 March	4 May
India	25 March	–
Ireland	12 March	18 May
Italy	9 March	18 May
Latvia	13 March	12 May
Lithuania	16 March	18 June
Luxembourg	15 March	20 April
North Macedonia	22 March	12 April
Malta	12 March	4 May
The Netherlands	23 March	11 May
Norway	12 March	11 May
Poland	13 March	11 April
Portugal	19 March	2 April
Romania	25 March	12 May
Serbia	15 March	21 April
Slovakia	16 March	22 April
Slovenia	16 March	20 April
Spain	14 March	9 May
Switzerland	13 March	27 April
Thailand	25 March	–
United Kingdom	23 March	–
United States	19 March	13 April

Table A3. Monthly changes in NO_2 concentrations relative to the bias-corrected model predictions for cities in Asia and Australia. Values in italics denote values that are statistically different from business as usual ($p<0.001$ based on a Kolmogorov–Smirnov test).

Location	No.	Jan 2020	Feb 2020	Mar 2020	Apr 2020	May 2020	Jun 2020
Bangkok, Thailand	7	−7.8 % (−10.9 %−−4.6 %)	−11.5 % (−15.3 %−−7.7 %)	−20.4 % (−25.9 %−−14.9 %)	−27.4 % (−31.8 %−−23.0 %)	−39.1 % (−43.6 %−−34.5 %)	−25.7 % (−30.7 %−−20.7 %)
Beijing, China	5	−21.1 % (−23.3 %−−19.1 %)	−38.8 % (−41.2 %−−36.3 %)	−31.7 % (−34.6 %−−28.7 %)	−25.0 % (−28.7 %−−21.4 %)	−23.8 % (−27.5 %−−20.2 %)	−20.4 % (−24.1 %−−16.6 %)
Chongqing, China	16	−11.1 % (−13.0 %−−9.2 %)	−38.4 % (−40.5 %−−36.3 %)	−11.6 % (−13.6 %−−9.5 %)	−0.1 % (−2.1 %−−1.9 %)	4.3 % (2.0 %−6.5 %)	3.5 % (1.1 %−6.0 %)
Guangzhou, China	11	−16.6 % (−19.5 %−−13.7 %)	−31.8 % (−35.1 %−−28.4 %)	−13.6 % (−16.7 %−−10.5 %)	−5.6 % (−8.7 %−−2.5 %)	−11.5 % (−15.6 %−−7.5 %)	−5.8 % (−11.1 %−−0.6 %)
Hong Kong, China	16	−6.9 % (−8.8 %−−4.9 %)	−13.9 % (−16.0 %−−11.8 %)	−3.7 % (−5.8 %−−1.6 %)	−4.1 % (−6.1 %−−2.1 %)	−4.7 % (−6.9 %−−2.4 %)	−12.8 % (−15.7 %−−10.0 %)
Melbourne, Australia	2	4.6 % (−5.6 %−14.8 %)	1.5 % (−9.1 %−12.1 %)	−7.6 % (−16.5 %−1.4 %)	−13.9 % (−21.9 %−−5.8 %)	−11.9 % (−19.3 %−−4.9 %)	−7.8 % (−14.1 %−−1.6 %)
Osaka, Japan	90	−14.4 % (−15.4 %−−13.4 %)	−6.4 % (−7.3 %−−5.5 %)	−13.4 % (−14.3 %−−12.5 %)	−25.7 % (−26.8 %−−24.7 %)	−28.1 % (−29.2 %−−27.0 %)	−17.4 % (−18.6 %−−16.3 %)
Shanghai, China	9	−14.4 % (−16.5 %−−12.3 %)	−39.8 % (−42.1 %−−37.5 %)	−23.3 % (−25.7 %−−20.8 %)	−19.3 % (−21.7 %−−17.0 %)	−5.5 % (−8.4 %−−2.7 %)	−1.9 % (−5.0 %−−1.2 %)
Taipei, Taiwan	18	−7.8 % (−9.4 %−−6.2 %)	−6.4 % (−8.0 %−−4.8 %)	−5.1 % (−6.7 %−−3.6 %)	−2.0 % (−3.6 %−−0.3 %)	−3.0 % (−4.7 %−−1.2 %)	−11.1 % (−13.0 %−−9.3 %)
Tianjin, China	10	−7.2 % (−8.7 %−−5.8 %)	−32.1 % (−34.0 %−−30.3 %)	−14.5 % (−16.5 %−−12.4 %)	−8.4 % (−10.9 %−−5.9 %)	−1.0 % (−3.7 %−1.7 %)	−2.5 % (−5.5 %−−0.6 %)
Tokyo, Japan	79	1.6 % (0.5 %−2.7 %)	−2.5 % (−3.6 %−−1.4 %)	−13.9 % (−15.1 %−−12.8 %)	−21.3 % (−22.5 %−−20.1 %)	−26.7 % (−28.0 %−−25.5 %)	−12.0 % (−13.3 %−−10.6 %)
Wuhan, China	9	−20.4 % (−23.6 %−−17.3 %)	−56.3 % (−59.4 %−−53.2 %)	−51.4 % (−54.6 %−−48.2 %)	−22.0 % (−25.3 %−−18.7 %)	−15.0 % (−18.7 %−−11.2 %)	−11.1 % (−15.9 %−−6.2 %)

Table A4. Monthly changes in NO_2 concentrations relative to the bias-corrected model predictions for cities in Europe. Values in italics denote values that are statistically different from business as usual ($p < 0.001$ based on a Kolmogorov–Smirnov test).

Location	No.	Jan 2020	Feb 2020	Mar 2020	Apr 2020	May 2020	Jun 2020
Amsterdam, Netherlands	1	−1.5 % (−8.2 %–5.3 %)	−8.5 % (−17.4 %–−0.4 %)	−16.2 % (−25.7 %–−6.4 %)	−27.2 % (−36.8 %–−17.6 %)	−18.4 % (−29.9 %–−6.9 %)	−17.2 % (−28.2 %–−6.3 %)
Athens, Greece	11	*13.8 % (11.4 %–16.1 %)*	1.9 % (−0.2 %–4.1 %)	−5.0 % (−7.1 %–−3.0 %)	−26.4 % (−28.7 %–−24.2 %)	−8.8 % (−10.9 %–−6.7 %)	−12.7 % (−15.0 %–−10.5 %)
Belgrade, Serbia	1	2.8 % (−5.1 %–10.7 %)	−10.6 % (−19.8 %–−1.4 %)	−40.9 % (−50.2 %–−31.6 %)	−71.7 % (−81.4 %–−62.0 %)	−31.0 % (−44.1 %–−17.8 %)	−17.0 % (−33.4 %–−0.6 %)
Berlin, Germany	18	2.1 % (0.4 %–3.8 %)	−7.3 % (−9.4 %–−5.2 %)	−9.7 % (−11.6 %–−7.8 %)	−25.3 % (−27.3 %–−23.3 %)	−12.6 % (−15.0 %–−10.2 %)	−15.4 % (−17.9 %–−12.9 %)
Bratislava, Slovakia	5	0.3 % (−2.8 %–3.3 %)	−15.7 % (−19.8 %–−11.5 %)	−18.3 % (−22.4 %–−14.3 %)	−18.2 % (−22.3 %–−14.2 %)	−12.4 % (−17.6 %–−7.1 %)	−14.9 % (−20.5 %–−9.3 %)
Brussels, Belgium	17	−5.2 % (−7.1 %–−3.4 %)	−11.8 % (−14.2 %–−9.3 %)	−25.4 % (−27.4 %–−23.4 %)	−40.8 % (−42.6 %–−39.0 %)	−30.7 % (−33.0 %–−28.5 %)	−19.7 % (−22.3 %–−17.0 %)
Bucharest, Romania	8	−1.7 % (−4.5 %–−1.0 %)	−9.9 % (−12.9 %–−7.0 %)	−21.6 % (−24.6 %–−18.6 %)	−39.8 % (−43.0 %–−36.5 %)	−23.3 % (−26.9 %–−19.8 %)	−23.0 % (−26.5 %–−19.5 %)
Budapest, Hungary	5	−2.2 % (−5.3 %–−0.8 %)	−9.2 % (−12.8 %–−5.5 %)	−12.0 % (−15.5 %–−8.6 %)	−23.6 % (−27.2 %–−20.0 %)	−24.4 % (−28.8 %–−20.0 %)	−25.7 % (−30.2 %–−21.3 %)
Copenhagen, Denmark	4	−1.7 % (−6.4 %–−2.9 %)	−9.6 % (−14.9 %–−4.3 %)	−19.0 % (−23.4 %–−14.7 %)	−25.7 % (−30.1 %–−21.4 %)	−18.7 % (−24.1 %–−13.3 %)	−13.8 % (−18.4 %–−9.1 %)
Dublin, Ireland	5	−8.7 % (−14.7 %–−2.7 %)	−9.3 % (−17.2 %–−1.5 %)	−28.8 % (−34.4 %–−23.1 %)	−39.2 % (−43.7 %–−34.8 %)	−38.0 % (−44.2 %–−31.8 %)	−40.8 % (−47.3 %–−34.2 %)
Helsinki, Finland	6	−9.1 % (−13.2 %–−4.9 %)	−15.2 % (−19.2 %–−11.1 %)	−18.2 % (−22.0 %–−14.5 %)	−38.8 % (−43.0 %–−34.5 %)	−33.0 % (−37.5 %–−28.6 %)	−25.9 % (−29.7 %–−22.2 %)
Lisbon, Portugal	20	−6.1 % (−8.1 %–−4.1 %)	−3.4 % (−5.3 %–−1.5 %)	−26.9 % (−29.4 %–−24.3 %)	−41.3 % (−44.1 %–−38.6 %)	−32.5 % (−35.4 %–−29.6 %)	−28.1 % (−32.0 %–−24.1 %)
Ljubljana, Slovenia	1	−3.8 % (−11.6 %–4.1 %)	−26.0 % (−33.7 %–−18.4 %)	−47.9 % (−56.2 %–−39.5 %)	−49.8 % (−59.1 %–−40.2 %)	−41.4 % (−53.1 %–−29.7 %)	−42.6 % (−54.2 %–−31.0 %)
London, United Kingdom	11	−3.6 % (−6.0 %–−1.1 %)	−4.3 % (−7.3 %–−1.2 %)	−17.0 % (−19.7 %–−14.3 %)	−35.9 % (−38.1 %–−33.6 %)	−35.1 % (−37.8 %–−32.3 %)	−28.8 % (−31.9 %–−25.8 %)
Luxembourg City, Luxembourg	9	*3.7 % (1.0 %–6.4 %)*	−3.4 % (−6.7 %–−0.1 %)	−24.4 % (−27.4 %–−21.4 %)	−40.2 % (−42.9 %–−37.6 %)	−27.0 % (−30.1 %–−23.9 %)	−19.2 % (−22.7 %–−15.7 %)
Madrid, Spain	37	*0.9 % (−0.5 %–2.4 %)*	−9.4 % (−10.8 %–−8.0 %)	−31.7 % (−33.6 %–−29.8 %)	−60.6 % (−62.6 %–−58.6 %)	−51.8 % (−54.0 %–−49.6 %)	−40.4 % (−42.8 %–−38.0 %)
Milan, Italy	19	*10.0 % (8.8 %–11.2 %)*	−2.0 % (−3.6 %–−0.3 %)	−25.7 % (−27.2 %–−24.2 %)	−41.6 % (−43.3 %–−39.9 %)	−34.7 % (−36.9 %–−32.6 %)	−24.4 % (−26.6 %–−22.1 %)
Oslo, Norway	12	−6.9 % (−9.3 %–−4.5 %)	−16.0 % (−18.5 %–−13.5 %)	−25.4 % (−28.1 %–−22.6 %)	−26.3 % (−29.4 %–−23.2 %)	−18.8 % (−22.4 %–−15.2 %)	−12.2 % (−15.7 %–−8.7 %)
Paris, France	28	−3.2 % (−4.5 %–−1.8 %)	−12.7 % (−14.4 %–−11.0 %)	−28.0 % (−29.5 %–−26.6 %)	−46.6 % (−48.0 %–−45.2 %)	−35.7 % (−37.3 %–−34.1 %)	−21.1 % (−22.9 %–−19.3 %)
Prague, Czech Republic	9	*3.9 % (1.6 %–6.2 %)*	−9.1 % (−12.1 %–−6.0 %)	−10.1 % (−12.6 %–−7.5 %)	−16.6 % (−19.0 %–−14.2 %)	−16.7 % (−19.5 %–−13.9 %)	−17.7 % (−20.6 %–−14.8 %)
Reykjavik, Iceland	3	−20.9 % (−28.3 %–−13.5 %)	−17.4 % (−23.8 %–−10.9 %)	−20.0 % (−27.4 %–−12.6 %)	−28.1 % (−36.3 %–−19.9 %)	6.7 % (−17.5 %–−3.0 %)	−0.2 % (−9.9 %–−9.4 %)
Riga, Latvia	1	−5.7 % (−17.6 %–6.3 %)	−7.6 % (−20.5 %–−5.3 %)	−23.9 % (−35.1 %–−12.7 %)	−45.5 % (−60.5 %–−30.6 %)	−48.9 % (−62.8 %–−35.0 %)	−12.6 % (−25.0 %–−0.2 %)
Rome, Italy	15	NA	−0.9 % (−3.3 %–−1.5 %)	−32.3 % (−34.3 %–−30.2 %)	−50.0 % (−52.1 %–−47.8 %)	−39.3 % (−41.6 %–−36.9 %)	−24.2 % (−26.8 %–−21.7 %)
Skopje, North Macedonia	1	−9.5 % (−17.5 %–−2.5 %)	*5.6 % (−2.9 %–14.3 %)*	−8.1 % (−16.6 %–−0.3 %)	−35.5 % (−43.9 %–−27.2 %)	−32.2 % (−41.7 %–−22.7 %)	−18.0 % (−27.8 %–−8.2 %)
Sofia, Bulgaria	4	*8.5 % (3.8 %–13.2 %)*	−3.4 % (−8.4 %–−1.6 %)	−16.5 % (−21.8 %–−11.2 %)	−27.3 % (−34.7 %–−19.9 %)	−20.3 % (−29.4 %–−11.1 %)	−10.7 % (−18.4 %–−3.5 %)
Stockholm, Sweden	6	−11.1 % (−15.4 %–−6.8 %)	−11.8 % (−15.8 %–−.8 %)	−18.0 % (−22.0 %–−14.1 %)	−33.0 % (−37.1 %–−28.9 %)	−23.7 % (−28.0 %–−19.4 %)	−20.9 % (−26.0 %–−25.5 %)
Tallinn, Estonia	3	−3.2 % (−12.0 %–−5.6 %)	−12.3 % (−21.3 %–−3.3 %)	−14.8 % (−24.1 %–−5.4 %)	−25.2 % (−34.3 %–−16.0 %)	−22.3 % (−31.4 %–−13.5 %)	−9.7 % (−17.3 %–−2.1 %)
Vienna, Austria	28	−2.3 % (−3.6 %–−0.9 %)	−14.4 % (−16.3 %–−12.6 %)	−20.6 % (−22.3 %–−18.9 %)	−26.2 % (−27.9 %–−24.5 %)	−16.5 % (−18.8 %–−14.2 %)	−25.4 % (−27.6 %–−23.1 %)
Vilnius, Lithuania	4	−11.8 % (−16.7 %–−7.0 %)	−3.5 % (−8.7 %–−1.7 %)	−10.1 % (−15.0 %–−5.2 %)	−24.4 % (−29.8 %–−18.9 %)	−16.2 % (−22.2 %–−10.2 %)	−20.3 % (−26.9 %–−13.7 %)
Warsaw, Poland	7	−10.4 % (−13.1 %–−7.6 %)	−15.7 % (−18.7 %–−12.6 %)	−15.2 % (−18.0 %–−12.4 %)	−26.0 % (−28.9 %–−23.1 %)	−18.3 % (−21.6 %–−15.1 %)	−17.5 % (−21.4 %–−13.6 %)
Zagreb, Croatia	3	*8.0 % (2.6 %–13.4 %)*	−15.2 % (−21.1 %–−9.4 %)	−32.0 % (−38.0 %–−25.9 %)	−51.5 % (−57.7 %–−45.2 %)	−50.0 % (−56.7 %–−43.3 %)	−42.3 % (−50.2 %–−34.4 %)
Zurich, Switzerland	8	*2.2 % (0.0 %–4.5 %)*	−11.8 % (−14.9 %–−8.6 %)	−15.1 % (−17.9 %–−12.3 %)	−28.0 % (−30.9 %–−25.2 %)	−23.4 % (−27.0 %–−19.8 %)	−25.5 % (−29.1 %–−22.0 %)

NA: not available.

Table A5. Monthly changes in NO_2 concentrations relative to the bias-corrected model predictions for cities in North America and South America. Values in italics denote values that are statistically different from business as usual ($p < 0.001$ based on a Kolmogorov–Smirnov test).

Location	No.	Jan 2020	Feb 2020	Mar 2020	Apr 2020	May 2020	Jun 2020
Atlanta, USA	3	9.7 % (4.6 %–14.9 %)	0.8 % (−4.5 %–6.2 %)	−3.3 % (−8.7 %– −2.2 %)	−12.4 % (−17.9 %– −6.9 %)	−6.7 % (−12.5 %– −1.2 %)	−7.1 % (−13.5 %– −1.1 %)
Boston, USA	4	−8.4 % (−12.5 %– −4.8 %)	−5.1 % (−9.2 %– −1.4 %)	−20.7 % (−25.8 %– −15.7 %)	−23.4 % (−29.3 %– −17.4 %)	−27.0 % (−33.4 %– −20.6 %)	−14.7 % (−20.6 %– −8.4 %)
Denver, USA	4	−4.5 % (−7.5 %– −1.9 %)	−7.5 % (−11.1 %– −4.3 %)	−20.5 % (−24.6 %– −16.5 %)	−21.2 % (−26.1 %– −16.3 %)	−35.8 % (−41.3 %– −30.4 %)	−24.1 % (−29.5 %– −18.7 %)
Edmonton, Canada	3	−4.0 % (−7.5 %– −0.7 %)	−11.5 % (−15.3 %– −7.6 %)	−15.2 % (−20.1 %– −10.3 %)	−18.0 % (−24.5 %– −11.4 %)	−34.9 % (−43.5 %– −26.3 %)	−32.3 % (−41.1 %– −23.5 %)
Honolulu, USA	1	−3.1 % (−16.1 %– −10.0 %)	−0.9 % (−15.6 %–13.9 %)	−11.7 % (−26.2 %–2.8 %)	−28.3 % (−42.2 %– −14.3 %)	−30.6 % (−47.0 %– −14.3 %)	−26.7 % (−42.7 %– −10.6 %)
Los Angeles, USA	8	4.7 % (2.8 %–6.9 %)	−4.1 % (−6.3 %– −1.9 %)	−11.9 % (−15.1 %– −8.7 %)	−28.2 % (−31.7 %– −24.8 %)	−27.5 % (−31.2 %– −24.2 %)	−23.4 % (−27.6 %– −19.3 %)
Medellín, Colombia	4	−2.0 % (−6.6 %–2.6 %)	11.6 % (7.1 %–16.0 %)	−7.1 % (−12.1 %– −2.6 %)	−51.9 % (−56.3 %– −47.8 %)	−24.8 % (−29.5 %– −20.1 %)	−21.1 % (−26.2 %– −16.1 %)
Miami, USA	3	−4.1 % (−14.5 %– −6.3 %)	−22.6 % (−32.8 %– −12.4 %)	−12.9 % (−21.7 %– −4.2 %)	−29.2 % (−40.9 %– −17.4 %)	NA	NA
Montréal, Canada	5	−5.4 % (−8.9 %– −2.1 %)	−4.4 % (−8.3 %– −0.8 %)	−22.9 % (−27.4 %– −18.7 %)	−36.4 % (−42.5 %– −30.7 %)	−25.8 % (−32.5 %– −19.1 %)	−14.7 % (−21.3 %– −8.1 %)
New York, USA	4	−5.5 % (−9.1 %– −2.4 %)	−8.0 % (−11.4 %– −4.8 %)	−20.8 % (−24.6 %– −17.0 %)	−29.7 % (−34.2 %– −25.2 %)	−25.1 % (−30.4 %– −19.8 %)	−17.1 % (−23.5 %– −10.7 %)
Oklahoma City, USA	2	−0.9 % (−6.9 %–45.0 %)	−3.5 % (−10.4 %–3.4 %)	−7.1 % (−13.6 %– −1.3 %)	−2.8 % (−9.5 %–3.8 %)	−13.9 % (−20.3 %– −7.4 %)	−8.0 % (−13.9 %– −2.2 %)
Phoenix, USA	5	−9.5 % (−12.0 %– −7.2 %)	−12.6 % (−15.7 %– −9.5 %)	−19.8 % (−23.6 %– −16.0 %)	−22.2 % (−26.3 %– −18.1 %)	−13.8 % (−18.1 %– −9.5 %)	−11.0 % (−16.1 %– −6.0 %)
Quito, Ecuador	8	−10.7 % (−13.9 %– −7.6 %)	2.5 % (−0.5 %–5.4 %)	−34.7 % (−37.5 %– −31.8 %)	−64.3 % (−67.2 %– −61.4 %)	−55.8 % (−58.8 %– −52.7 %)	−24.9 % (−27.9 %– −21.8 %)
Rio de Janeiro, Brazil	2	−4.9 % (−11.5 %– −1.7 %)	0.8 % (−5.7 %–7.2 %)	−5.2 % (−11.9 %–1.5 %)	−15.9 % (−22.6 %– −9.2 %)	6.5 % (1.5 %–12.2 %)	4.4 % (−0.5 %–9.4 %)
Salt Lake City, USA	3	−1.4 % (−5.0 %– −2.2 %)	−5.5 % (−9.8 %– −1.9 %)	−15.4 % (−21.2 %– −9.8 %)	−24.7 % (−31.9 %– −17.4 %)	−28.3 % (−36.5 %– −20.0 %)	−20.6 % (−29.6 %– −11.6 %)
San Francisco, USA	7	4.6 % (2.1 %–7.2 %)	−1.8 % (−4.4 %– −0.7 %)	−14.8 % (−18.1 %– −11.5 %)	−26.7 % (−30.8 %– −22.6 %)	−18.4 % (−22.7 %– −14.0 %)	−15.7 % (−20.6 %– −10.8 %)
Santiago de Chile, Chile	4	−6.6 % (−16.9 %–3.6 %)	−10.5 % (−19.2 %– −1.8 %)	−8.4 % (−16.4 %– −1.1 %)	−20.9 % (−26.8 %– −14.9 %)	−11.8 % (−16.7 %– −7.0 %)	−6.9 % (−11.9 %– −1.8 %)
Seattle, USA	1	−8.6 % (−18.0 %– −0.9 %)	−2.5 % (−11.7 %–6.7 %)	−12.7 % (−22.4 %– −2.9 %)	−34.0 % (−44.7 %– −23.2 %)	−28.9 % (−41.6 %– −16.7 %)	−19.8 % (−33.6 %– −6.1 %)
St. Louis, USA	3	−4.4 % (−9.4 %– −0.6 %)	−11.9 % (−17.3 %– −6.6 %)	−16.4 % (−21.7 %– −11.1 %)	−24.8 % (−31.1 %– −18.6 %)	−23.9 % (−30.4 %– −17.4 %)	−23.8 % (−30.0 %– −17.6 %)
Washington D.C., USA	7	−7.0 % (−9.9 %– −4.0 %)	−10.0 % (−13.1 %– −6.9 %)	−18.4 % (−21.9 %– −14.8 %)	−22.3 % (−26.4 %– −18.2 %)	−25.2 % (−30.0 %– −20.3 %)	−14.6 % (−19.4 %– −9.9 %)

NA: not available.

Table A6. Monthly changes in O_3 concentrations relative to the bias-corrected model predictions for cities in Asia and Australia. Values in italics denote values that are statistically different from business as usual ($p < 0.001$ based on a Kolmogorov–Smirnov test).

Location	No.	Jan 2020	Feb 2020	Mar 2020	Apr 2020	May 2020	Jun 2020
Bangkok, Thailand	6	−6.1 % (−9.4 %−−2.8 %)	−2.8 % (−6.1 %−0.5 %)	−10.2 % (−13.9 %−−6.5 %)	11.2 % (7.4 %−15.1 %)	3.6 % (−2.1 %−9.2 %)	34.7 % (28.0 %−41.3 %)
Beijing, China	5	10.9 % (6.2 %−15.6 %)	1.4 % (−2.2 %−4.9 %)	1.7 % (−1.1 %−4.5 %)	11.7 % (9.4 %−14.0 %)	−4.4 % (−6.1 %−2.3 %)	9.5 % (8.1 %−11.0 %)
Chongqing, China	16	−3.6 % (−7.0 %−0.3 %)	−2.4 % (−4.9 %−0.1 %)	4.3 % (2.6 %−5.9 %)	3.1 % (1.6 %−4.6 %)	6.9 % (5.8 %−8.1 %)	2.1 % (0.8 %−3.3 %)
Guangzhou, China	11	−0.9 % (−3.4 %−1.7 %)	5.0 % (2.3 %−7.8 %)	−15.4 % (−18.0 %−−12.9 %)	4.8 % (2.6 %−7.0 %)	11.3 % (9.4 %−13.2 %)	−1.5 % (−3.8 %−0.9 %)
Hong Kong, China	16	−0.1 % (−2.7 %−2.6 %)	−8.3 % (−10.9 %−−5.6 %)	−2.9 % (−5.6 %−−0.2 %)	−2.3 % (−4.8 %−0.1 %)	9.0 % (5.0 %−12.9 %)	−4.5 % (−10.3 %−1.4 %)
Melbourne, Australia	3	1.1 % (−3.7 %−6.0 %)	−8.9 % (−14.4 %−−3.4 %)	3.7 % (−1.6 %−8.9 %)	2.7 % (−2.5 %−7.9 %)	−6.1 % (−11.6 %−0.7 %)	−19.6 % (−25.1 %−−14.1 %)
Osaka, Japan	57	12.7 % (11.3 %−14.2 %)	−3.6 % (−4.8 %−−2.4 %)	1.4 % (0.4 %−2.3 %)	11.4 % (10.7 %−12.2 %)	3.3 % (2.5 %−4.0 %)	1.2 % (0.3 %−2.1 %)
Shanghai, China	9	−2.9 % (−5.2 %−−0.5 %)	5.8 % (3.7 %−7.9 %)	0.6 % (−1.0 %−2.2 %)	11.4 % (9.9 %−12.9 %)	2.1 % (0.9 %−3.3 %)	1.5 % (−0.0 %−3.0 %)
Taipei, Taiwan	16	−0.9 % (−2.4 %−0.6 %)	−9.9 % (−11.3 %−−8.6 %)	−8.0 % (−9.2 %−−6.8 %)	−9.6 % (−10.6 %−−8.6 %)	−6.6 % (−8.0 %−−5.1 %)	−5.2 % (−7.1 %−−3.3 %)
Tianjin, China	10	5.9 % (2.6 %−9.2 %)	−8.1 % (−10.5 %−−5.8 %)	−1.4 % (−3.4 %−0.6 %)	14.1 % (12.4 %−15.8 %)	−8.4 % (−9.7 %−−7.2 %)	7.3 % (6.1 %−8.5 %)
Tokyo, Japan	42	−4.5 % (−6.3 %−−2.7 %)	1.7 % (0.2 %−3.3 %)	0.3 % (−0.9 %−1.4 %)	6.4 % (5.4 %−7.4 %)	3.8 % (2.8 %−4.8 %)	−1.4 % (−2.6 %−−0.3 %)
Wuhan, China	9	8.6 % (4.7 %−12.4 %)	12.3 % (9.7 %−14.9 %)	4.3 % (2.3 %−6.3 %)	10.4 % (8.7 %−12.0 %)	−2.4 % (−3.7 %−−1.1 %)	−8.2 % (−9.7 %−−6.7 %)

Table A7. Monthly changes in O$_3$ concentrations relative to the bias-corrected model predictions for cities in Europe. Values in italics denote values that are statistically different from business as usual ($p<0.001$ based on a Kolmogorov–Smirnov test).

Location	No.	Jan 2020	Feb 2020	Mar 2020	Apr 2020	May 2020	Jun 2020
Amsterdam, Netherlands	1	21.6 % (11.6 %–31.6 %)	11.4 % (5.9 %–16.9 %)	22.5 % (16.9 %–28.1 %)	26.4 % (21.1 %–31.6 %)	7.1 % (2.7 %–11.4 %)	−3.7 % (−8.1 %–−0.7 %)
Athens, Greece	10	1.0 % (−1.3 %–3.2 %)	4.3 % (1.9 %–6.6 %)	0.0 % (−1.9 %–2.0 %)	4.4 % (2.6 %–6.1 %)	−3.9 % (−5.5 %–−2.2 %)	−5.7 % (−7.3 %–−4.0 %)
Belgrade, Serbia	1	−25.2 % (−39.7 %–−10.8 %)	0.9 % (−7.3 %–9.1 %)	15.2 % (9.0 %–21.5 %)	15.0 % (10.1 %–19.9 %)	−5.5 % (−10.5 %–−0.5 %)	−14.3 % (−19.8 %–−8.8 %)
Berlin, Germany	9	8.2 % (5.4 %–11.1 %)	7.3 % (5.5 %–9.2 %)	7.4 % (5.7 %–9.1 %)	1.8 % (0.6 %–3.1 %)	−6.2 % (−7.4 %–−4.9 %)	−9.0 % (−10.2 %–−7.7 %)
Bratislava, Slovakia	4	−7.1 % (−11.1 %–−3.1 %)	8.1 % (5.7 %–10.5 %)	6.1 % (4.1 %–8.2 %)	1.3 % (−0.3 %–2.9 %)	−3.2 % (−4.8 %–−1.3 %)	−11.2 % (−12.9 %–−9.3 %)
Brussels, Belgium	7	8.7 % (5.6 %–11.9 %)	11.2 % (9.2 %–13.3 %)	16.7 % (14.5 %–18.8 %)	18.3 % (16.5 %–20.1 %)	2.9 % (1.3 %–4.5 %)	−5.9 % (−7.4 %–−4.3 %)
Bucharest, Romania	4	−12.3 % (−16.8 %–−7.8 %)	0.4 % (−3.1 %–3.8 %)	−11.8 % (−14.4 %–−9.2 %)	−9.1 % (−11.2 %–−6.9 %)	−13.3 % (−15.5 %–−11.2 %)	−3.6 % (−5.8 %–−0.8 %)
Budapest, Hungary	3	18.2 % (8.6 %–27.2 %)	20.1 % (15.8 %–24.4 %)	16.1 % (12.4 %–19.8 %)	4.4 % (1.6 %–7.3 %)	−2.7 % (−5.4 %–−0.0 %)	−13.1 % (−15.9 %–−10.2 %)
Copenhagen, Denmark	2	4.9 % (2.1 %–7.7 %)	5.1 % (3.0 %–7.3 %)	7.5 % (5.7 %–9.4 %)	1.8 % (0.1 %–3.5 %)	−2.4 % (−4.0 %–−0.5 %)	−5.2 % (−6.7 %–−3.2 %)
Dublin, Ireland	4	5.6 % (2.3 %–8.8 %)	−2.0 % (−4.6 %–−0.6 %)	2.7 % (−0.1 %–5.5 %)	8.7 % (5.6 %–11.5 %)	−1.9 % (−4.4 %–0.7 %)	−13.8 % (−16.7 %–−10.9 %)
Helsinki, Finland	2	5.5 % (0.9 %–10.1 %)	−0.3 % (−4.4 %–3.9 %)	−3.7 % (−7.5 %–−0.0 %)	−2.2 % (−5.5 %–1.1 %)	3.1 % (0.7 %–5.5 %)	−4.7 % (−7.1 %–−1.7 %)
Lisbon, Portugal	14	6.6 % (4.8 %–8.3 %)	−3.8 % (−5.5 %–−2.2 %)	2.6 % (1.5 %–3.7 %)	4.8 % (3.8 %–5.8 %)	−6.4 % (−7.4 %–−5.5 %)	−4.3 % (−5.4 %–−3.1 %)
Ljubljana, Slovenia	2	−4.9 % (−8.5 %–−0.9 %)	0.2 % (−2.5 %–2.9 %)	0.8 % (−1.5 %–3.0 %)	3.5 % (1.7 %–5.3 %)	−6.4 % (−8.3 %–−4.0 %)	−12.4 % (−14.4 %–−10.4 %)
London, United Kingdom	5	8.6 % (4.4 %–12.8 %)	5.6 % (2.8 %–8.3 %)	14.9 % (12.5 %–17.2 %)	20.3 % (17.9 %–22.7 %)	6.7 % (4.6 %–8.9 %)	−2.5 % (−4.7 %–−0.3 %)
Luxembourg City, Luxembourg	5	0.8 % (−2.5 %–4.2 %)	3.4 % (1.1 %–5.7 %)	13.0 % (10.9 %–15.2 %)	10.2 % (8.3 %–12.1 %)	−0.2 % (−2.0 %–1.5 %)	−9.5 % (−11.3 %–−7.8 %)
Madrid, Spain	26	0.7 % (−1.3 %–2.7 %)	−9.2 % (−11.1 %–−7.3 %)	4.7 % (3.7 %–5.7 %)	6.4 % (5.5 %–7.3 %)	−2.2 % (−3.0 %–−1.5 %)	−6.1 % (−6.8 %–−5.4 %)
Milan, Italy	8	5.3 % (−8.6 %–19.2 %)	14.6 % (7.9 %–21.3 %)	22.6 % (19.1 %–26.1 %)	25.6 % (23.3 %–27.9 %)	0.7 % (−1.1 %–2.6 %)	−10.3 % (−12.0 %–−8.6 %)
Paris, France	11	5.7 % (2.9 %–8.5 %)	3.8 % (2.1 %–5.6 %)	14.5 % (12.8 %–16.3 %)	8.3 % (6.9 %–9.6 %)	2.5 % (1.2 %–3.7 %)	−6.2 % (−7.5 %–−4.9 %)
Prague, Czech Republic	6	−11.0 % (−14.6 %–−7.3 %)	10.8 % (8.5 %–13.0 %)	9.3 % (7.2 %–11.4 %)	6.9 % (5.2 %–8.6 %)	−2.6 % (−4.2 %–−1.0 %)	−12.6 % (−14.2 %–−11.1 %)
Riga, Latvia	1	−1.3 % (−6.1 %–3.5 %)	8.1 % (3.9 %–12.4 %)	11.7 % (7.9 %–15.5 %)	3.7 % (0.8 %–6.6 %)	32.6 % (28.2 %–37.1 %)	20.6 % (14.6 %–26.6 %)
Rome, Italy	9	NA	−5.1 % (−8.4 %–−1.7 %)	8.2 % (6.1 %–10.3 %)	15.4 % (13.4 %–17.3 %)	12.5 % (10.8 %–14.3 %)	−5.8 % (−7.4 %–−4.3 %)
Sofia, Bulgaria	4	3.7 % (0.3 %–7.2 %)	11.1 % (8.4 %–13.8 %)	10.6 % (8.5 %–12.7 %)	4.0 % (1.8 %–6.1 %)	4.7 % (2.8 %–6.7 %)	−3.8 % (−5.6 %–−1.8 %)
Stockholm, Sweden	2	5.8 % (2.5 %–9.0 %)	5.8 % (2.8 %–8.8 %)	0.6 % (−1.9 %–3.1 %)	−3.6 % (−5.7 %–−1.5 %)	−8.1 % (−10.5 %–−5.8 %)	−2.2 % (−4.4 %–−0.1 %)
Tallinn, Estonia	3	3.1 % (−0.5 %–6.7 %)	2.1 % (−1.1 %–5.2 %)	1.1 % (−1.9 %–4.1 %)	0.2 % (−2.4 %–2.8 %)	7.0 % (4.1 %–10.0 %)	−0.5 % (−3.6 %–2.7 %)
Vienna, Austria	11	−8.3 % (−10.8 %–−5.8 %)	8.0 % (6.4 %–9.6 %)	5.6 % (4.2 %–6.9 %)	3.9 % (2.8 %–5.0 %)	−4.5 % (−5.6 %–−3.4 %)	−11.1 % (−12.2 %–−10.0 %)
Vilnius, Lithuania	2	6.8 % (1.8 %–11.7 %)	1.2 % (−2.4 %–4.8 %)	−3.9 % (−6.9 %–−0.4 %)	−2.7 % (−5.0 %–−0.3 %)	−5.5 % (−8.1 %–−2.8 %)	−20.3 % (−22.9 %–−17.7 %)
Warsaw, Poland	7	3.3 % (−0.2 %–6.8 %)	8.9 % (6.5 %–11.4 %)	1.7 % (−0.3 %–3.7 %)	−2.5 % (−4.1 %–−0.8 %)	−13.9 % (−15.5 %–−12.4 %)	−21.3 % (−22.8 %–−19.8 %)
Zagreb, Croatia	2	−12.3 % (−22.6 %–−2.0 %)	17.3 % (11.1 %–23.5 %)	17.8 % (13.3 %–22.3 %)	15.3 % (11.4 %–19.1 %)	7.6 % (3.9 %–11.4 %)	−7.6 % (−11.3 %–−3.8 %)
Zurich, Switzerland	8	−12.6 % (−16.7 %–−8.6 %)	2.8 % (0.5 %–5.1 %)	7.3 % (5.1 %–9.6 %)	12.4 % (10.6 %–14.2 %)	−1.2 % (−2.8 %–0.5 %)	−6.9 % (−8.6 %–−5.2 %)

NA: not available.

Table A8. Monthly changes in O_3 concentrations relative to the bias-corrected model predictions for cities in North America and South America. Values in italics denote values that are statistically different from business as usual ($p < 0.001$ based on Kolmogorov–Smirnov test).

Location	No.	Jan 2020	Feb 2020	Mar 2020	Apr 2020	May 2020	Jun 2020
Atlanta, USA	1	NA	7.4 % (−8.5 %–23.2 %)	−3.4 % (−8.1 %–1.3 %)	−0.9 % (−4.7 %–3.0 %)	−3.9 % (−8.1 %–0.3 %)	−9.9 % (−14.5 %–−5.3 %)
Boston, USA	3	6.1 % (2.9 %–9.4 %)	8.4 % (5.4 %–11.3 %)	6.2 % (4.0 %–8.3 %)	1.9 % (−0.2 %–4.1 %)	−4.5 % (−6.6 %–2.1 %)	−7.9 % (−10.1 %–−5.6 %)
Denver, USA	4	7.3 % (4.1 %–10.6 %)	13.5 % (10.3 %–16.7 %)	−1.0 % (−3.4 %–1.5 %)	7.6 % (5.3 %–9.9 %)	6.1 % (4.1 %–8.1 %)	−0.6 % (−2.4 %–1.3 %)
Edmonton, Canada	3	0.5 % (−4.0 %–5.0 %)	1.0 % (−2.4 %–4.3 %)	−2.9 % (−5.2 %–−0.2 %)	3.1 % (1.2 %–5.1 %)	−7.7 % (−9.6 %–5.4 %)	−5.3 % (−7.8 %–−2.6 %)
Honolulu, USA	1	1.0 % (−2.3 %–4.4 %)	−6.7 % (−9.7 %–−3.2 %)	−9.2 % (−12.4 %–−5.6 %)	−6.4 % (−10.5 %–−2.3 %)	−18.0 % (−22.0 %–−14.1 %)	−15.9 % (−20.6 %–−11.2 %)
Los Angeles, USA	7	1.0 % (−1.9 %–3.9 %)	10.0 % (7.5 %–12.4 %)	−2.5 % (−4.5 %–−0.6 %)	−4.9 % (−6.6 %–−3.2 %)	−5.7 % (−7.3 %–−4.1 %)	−3.6 % (−5.2 %–−2.0 %)
Medellín, Colombia	5	1.3 % (−3.6 %–6.3 %)	−4.2 % (−8.1 %–−0.2 %)	*19.0 % (15.0 %–23.0 %)*	*26.0 % (21.0 %–31.0 %)*	8.5 % (3.1 %–13.9 %)	−14.8 % (−20.2 %–−9.4 %)
Miami, USA	2	3.2 % (−3.7 %–10.4 %)	−5.8 % (−10.9 %–−0.8 %)	1.2 % (−2.0 %–4.4 %)	−8.2 % (−12.7 %–−4.1 %)	NA	NA
Montréal, Canada	8	5.0 % (2.5 %–7.5 %)	6.0 % (3.8 %–8.1 %)	3.1 % (1.4 %–4.7 %)	3.6 % (2.0 %–5.2 %)	−2.8 % (−4.3 %–−1.3 %)	−9.2 % (−10.8 %–−7.6 %)
New York, USA	7	6.5 % (2.9 %–10.1 %)	*18.5 % (14.9 %–22.1 %)*	*15.1 % (12.8 %–17.4 %)*	*15.3 % (13.4 %–17.3 %)*	6.7 % (4.7 %–8.7 %)	−4.4 % (−6.3 %–−2.5 %)
Oklahoma City, USA	3	7.6 % (3.1 %–12.0 %)	9.1 % (6.1 %–12.2 %)	−4.0 % (−6.5 %–−1.4 %)	−3.8 % (−5.7 %–−1.8 %)	1.8 % (−0.6 %–3.8 %)	6.0 % (4.0 %–8.1 %)
Phoenix, USA	14	−2.5 % (−4.8 %–−0.3 %)	3.7 % (2.0 %–5.3 %)	3.0 % (1.6 %–4.4 %)	4.6 % (3.5 %–5.8 %)	0.3 % (−0.7 %–1.3 %)	−2.0 % (−3.0 %–−1.0 %)
Quito, Ecuador	8	−9.8 % (−13.2 %–−6.5 %)	−7.1 % (−10.1 %–−4.0 %)	6.3 % (3.4 %–9.1 %)	*37.4 % (33.7 %–41.1 %)*	*11.7 % (8.1 %–15.2 %)*	5.9 % (2.4 %–9.4 %)
Rio de Janeiro, Brazil	6	−7.2 % (−11.3 %–−3.2 %)	−5.7 % (−9.8 %–−1.6 %)	4.0 % (−0.1 %–8.1 %)	*23.9 % (19.6 %–28.2 %)*	*17.6 % (13.5 %–21.8 %)*	*11.3 % (7.0 %–15.7 %)*
Salt Lake City, USA	3	*29.6 % (22.6 %–36.6 %)*	12.3 % (7.5 %–17.2 %)	−1.4 % (−4.4 %–1.5 %)	1.1 % (−1.6 %–3.7 %)	3.1 % (0.8 %–5.5 %)	−2.0 % (−4.2 %–0.3 %)
San Francisco, USA	6	−0.9 % (−3.5 %–1.8 %)	8.5 % (5.9 %–11.0 %)	7.1 % (5.3 %–8.9 %)	−2.2 % (−3.9 %–−0.5 %)	3.6 % (1.8 %–5.5 %)	−3.4 % (−5.6 %–−1.3 %)
Santiago de Chile, Chile	3	−2.0 % (−5.8 %–1.7 %)	*−14.5 % (−18.6 %–−10.6 %)*	−6.9 % (−11.0 %–−2.7 %)	12.3 % (7.1 %–17.4 %)	6.7 % (0.3 %–13.1 %)	3.1 % (−7.2 %–13.4 %)
Seattle, USA	1	8.0 % (2.2 %–13.8 %)	−8.3 % (−14.2 %–−2.5 %)	4.9 % (−0.2 %–9.9 %)	5.2 % (0.7 %–9.7 %)	−3.4 % (−9.0 %–2.1 %)
St. Louis, USA	3	−5.3 % (−12.7 %–2.1 %)	9.5 % (5.4 %–13.6 %)	*−13.9 % (−16.9 %–−10.9 %)*	−7.3 % (−9.9 %–−4.7 %)	−6.6 % (−9.4 %–−4.0 %)	−3.5 % (−5.8 %–−0.8 %)
Washington D.C., USA	8	8.5 % (5.2 %–11.9 %)	*11.1 % (8.7 %–13.5 %)*	−2.2 % (−3.8 %–−0.6 %)	0.2 % (−1.3 %–1.7 %)	−3.6 % (−5.1 %–−2.1 %)	−1.3 % (−2.8 %–0.2 %)

NA: not available.
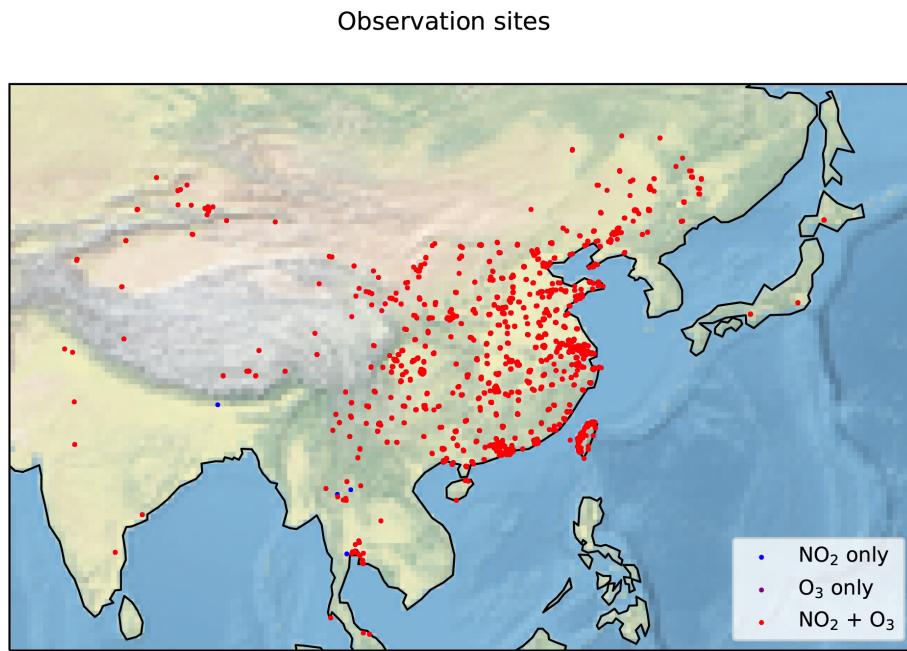
Observation sites

Figure A1. Close-up image of Chinese observation sites included in the analysis. Red points indicate sites with both NO_2 and O_3 observations, purple points show locations with O_3 observations only, and blue points show locations with NO_2 observations only.
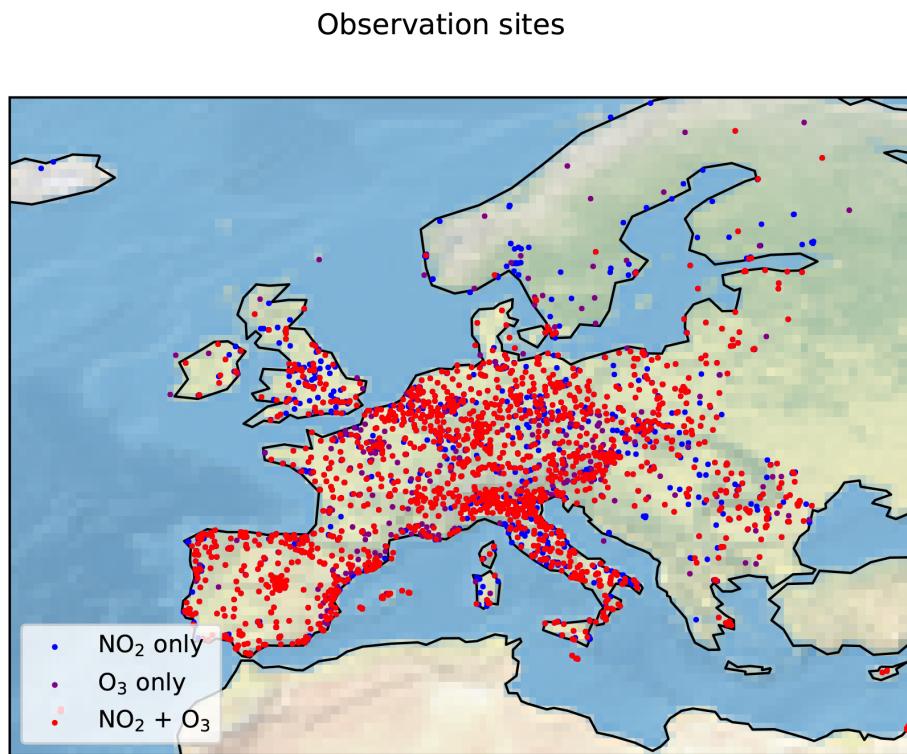
Observation sites

Figure A2. Close-up image of European observation sites included in the analysis. Red points indicate sites with both NO_2 and O_3 observations, purple points show locations with O_3 observations only, and blue points show locations with NO_2 observations only.
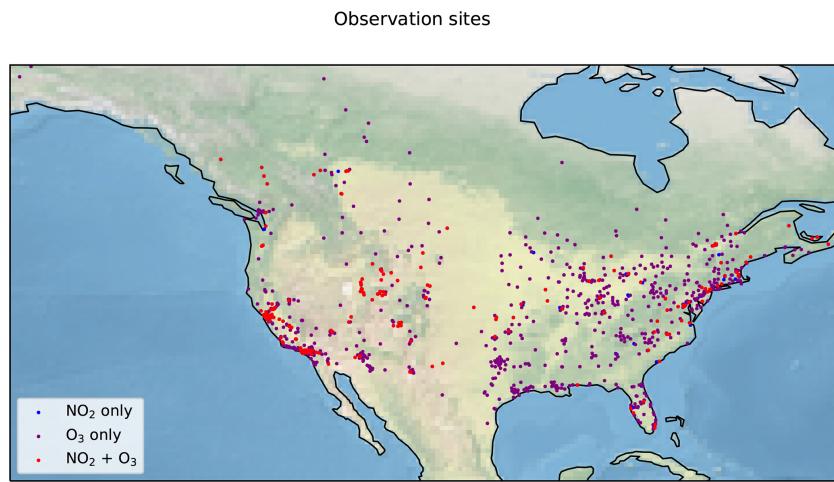
Observation sites

Figure A3. Close-up image of North American observation sites included in the analysis. Red points indicate sites with both NO_2 and O_3 observations, purple points show locations with O_3 observations only, and blue points show locations with NO_2 observations only.
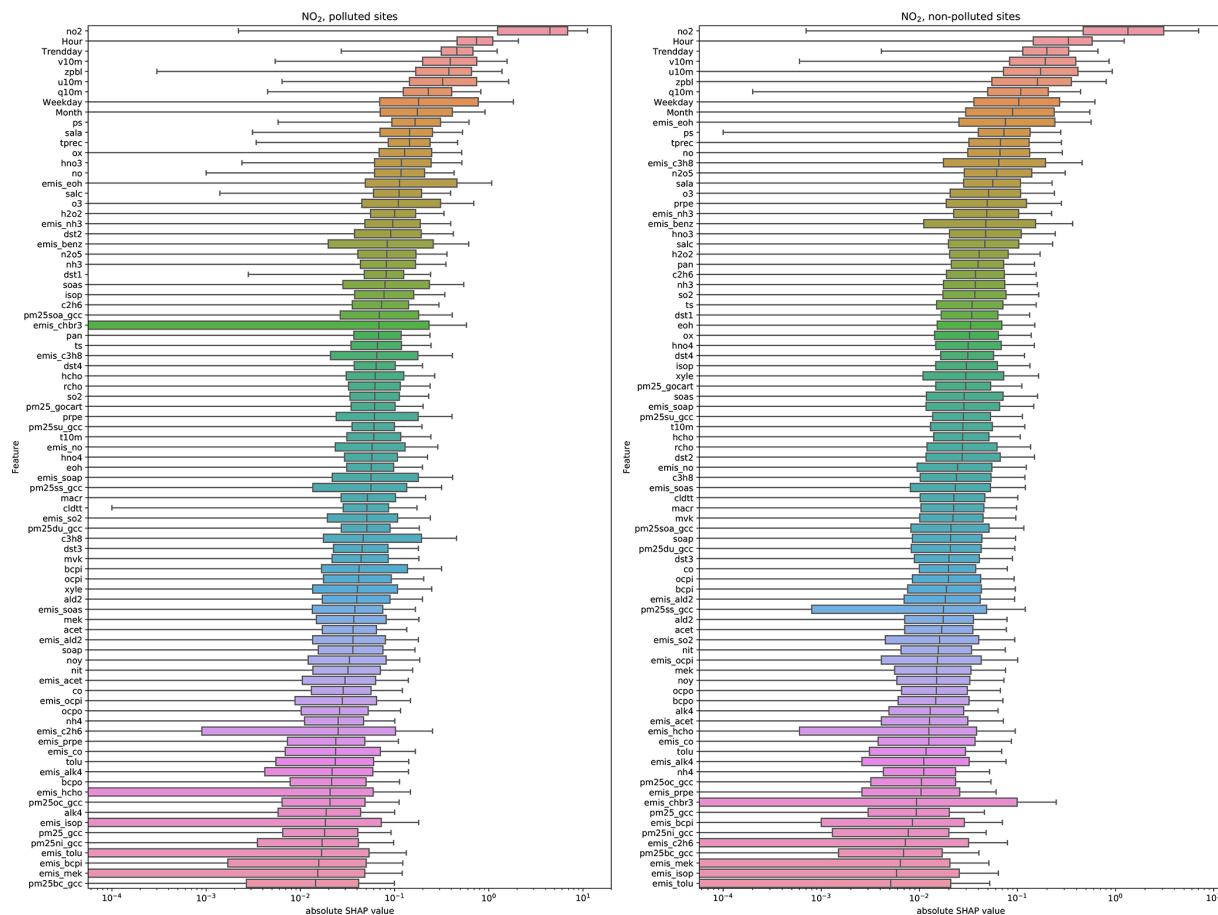
Figure A4. Importance of input variables (features) for the XGBoost models trained to predict NO_2 model bias. Shown are the distribution of the absolute SHAP values for each feature, ranked by the average importance of each feature. Higher SHAP value indicates higher feature importance. The left panel shows results for polluted sites (average annual NO_2 concentration >15 ppbv) and the right panel shows results for all other sites.
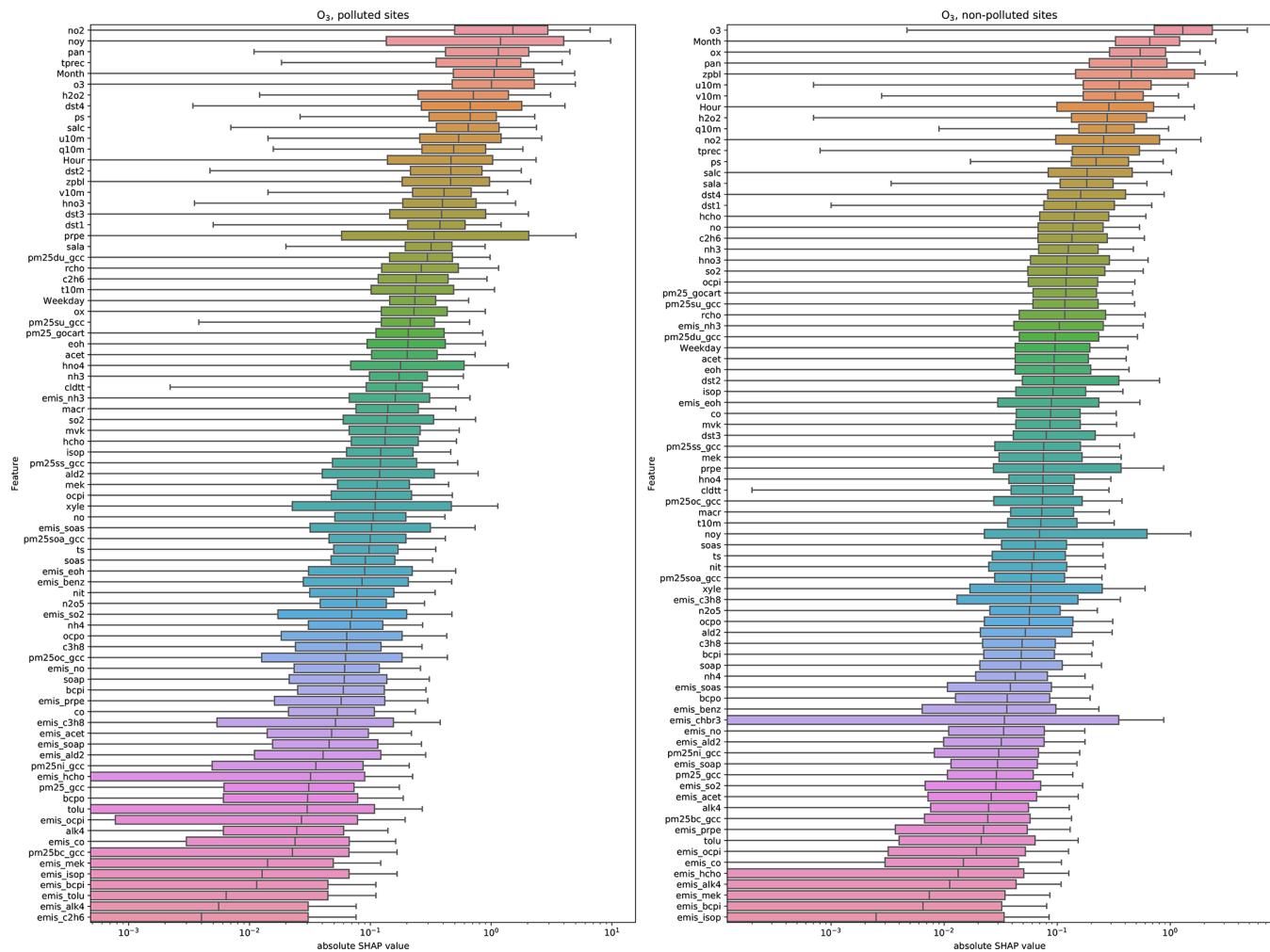
Figure A5. The same as Fig. A4 but for O$_3$.
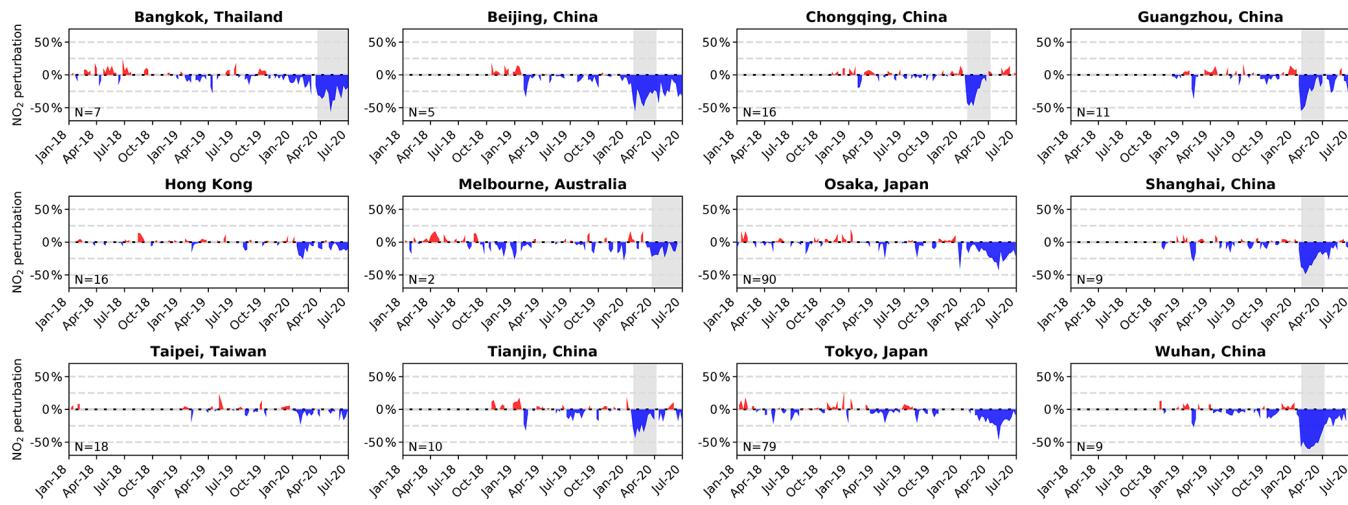
Figure A6. Normalized fractional NO$_2$ perturbations (observation–bias-corrected model, normalized by the bias-corrected model prediction) from 1 January 2018 through June 2020 for selected cities in Asia and Australia. Grey-shaded areas indicate COVID-19 lockdown periods. Number of sites per city are shown in the bottom left of each panel.
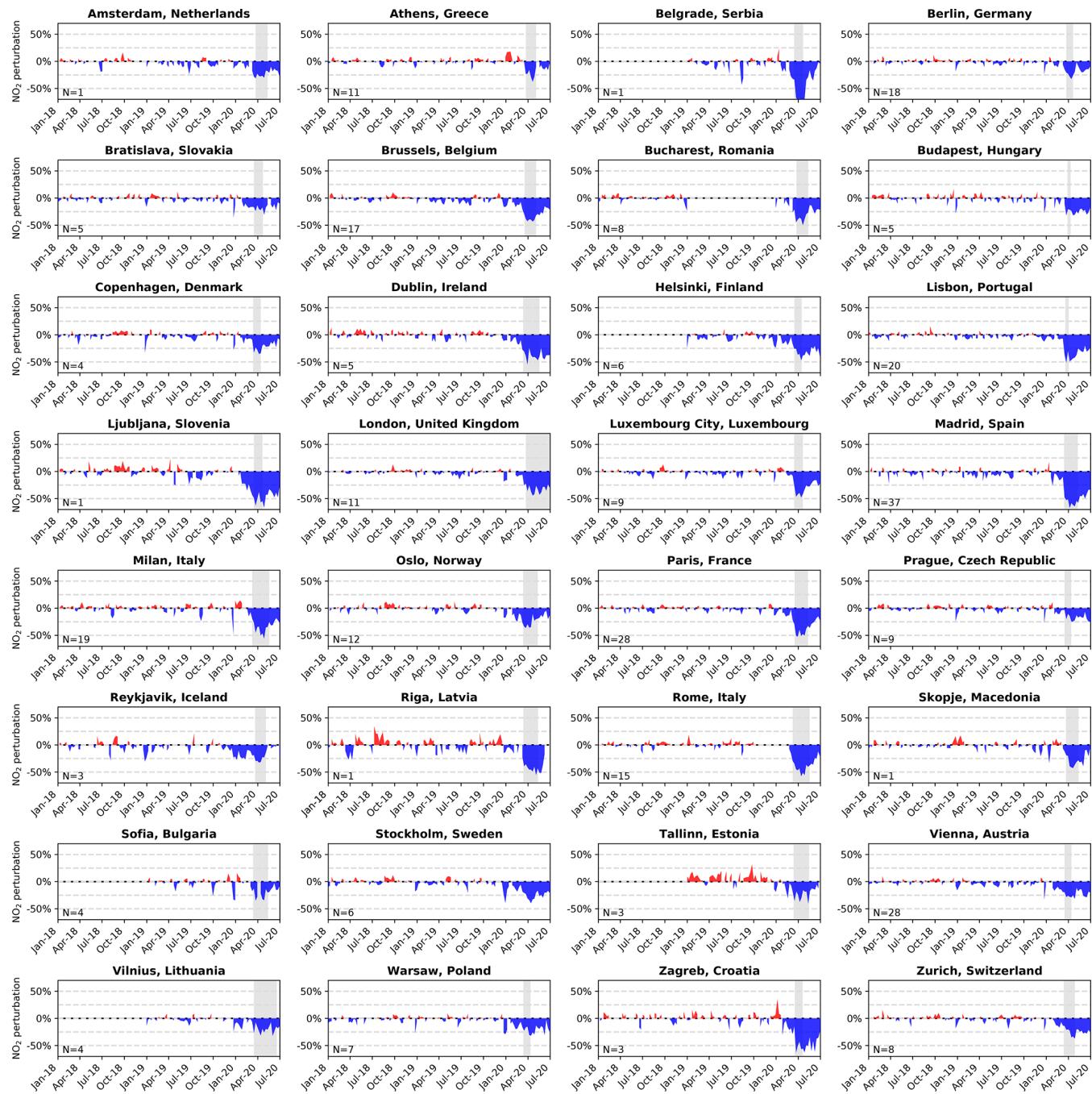
Figure A7. The same as Fig. A6 but for Europe.
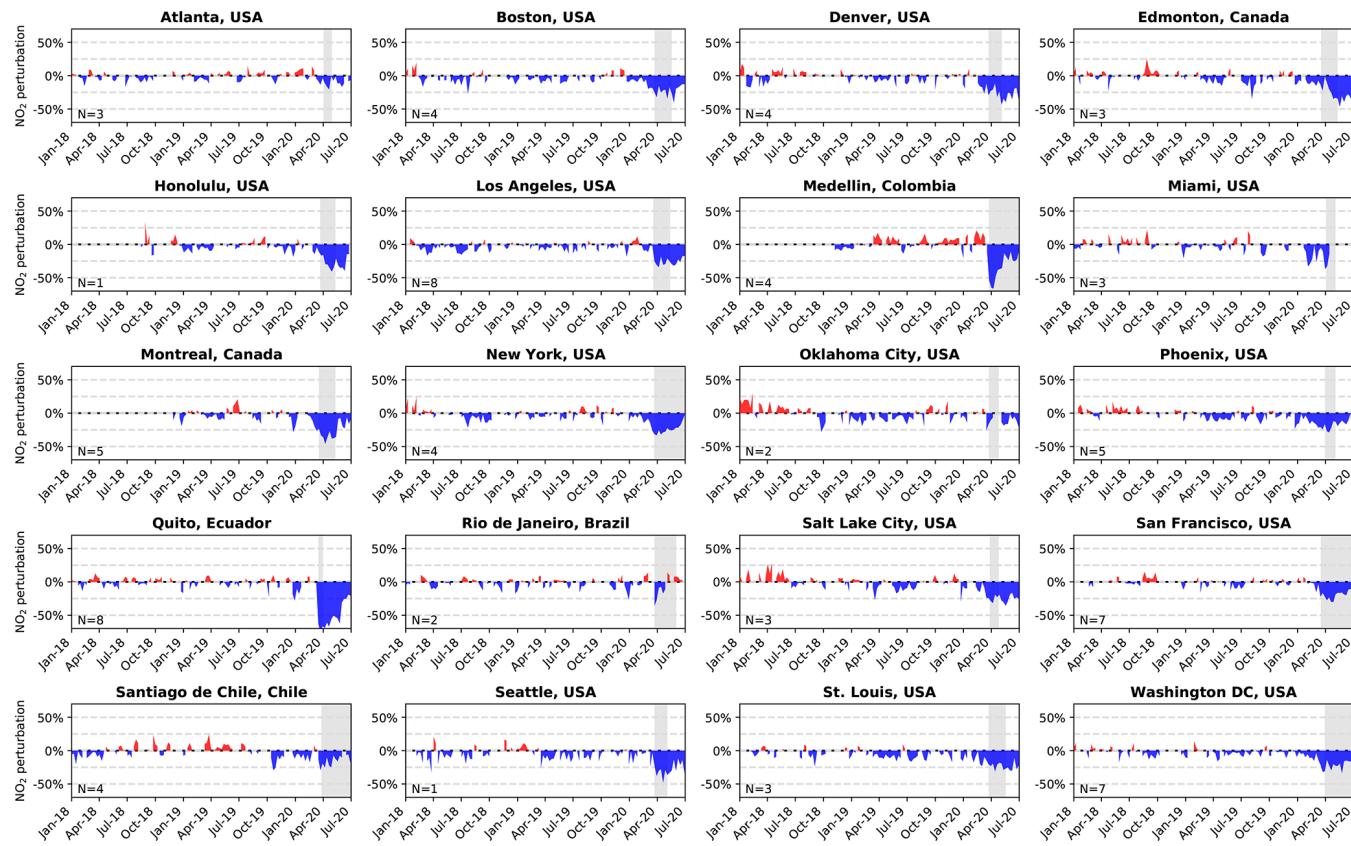
Figure A8. The same as Fig. A6 but for North and South America.
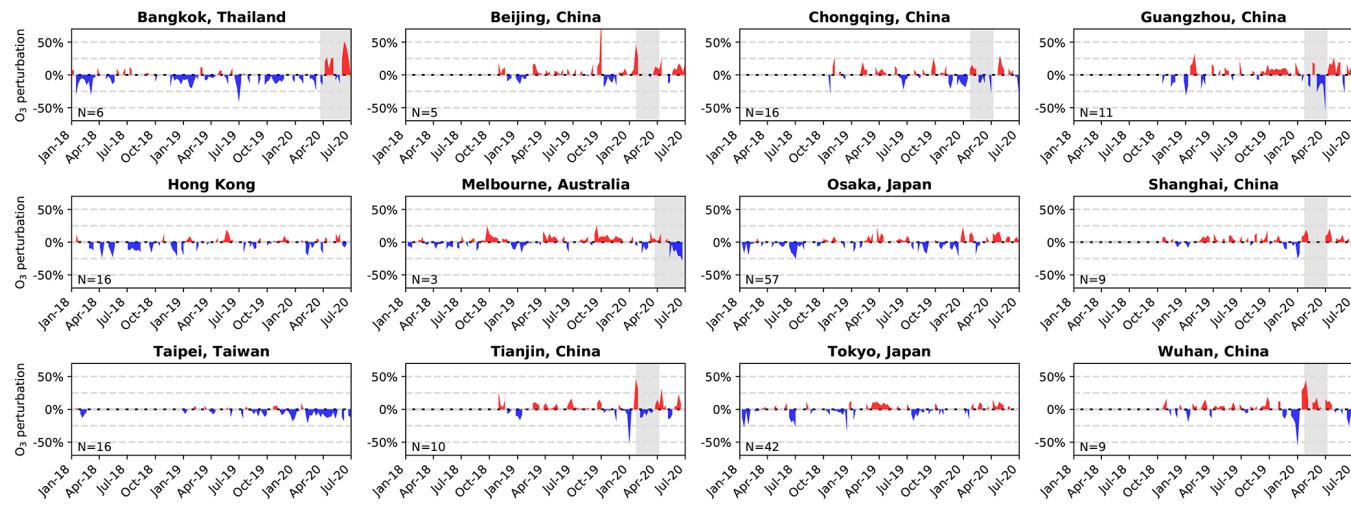
Figure A9. Normalized fractional O$_3$ perturbations (observation–bias-corrected model, normalized by the bias-corrected model prediction) from 1 January 2018 through June 2020 for selected cities in Asia and Australia. Grey-shaded areas indicate COVID-19 lockdown periods. Number of sites per city are shown in the bottom left of each panel.
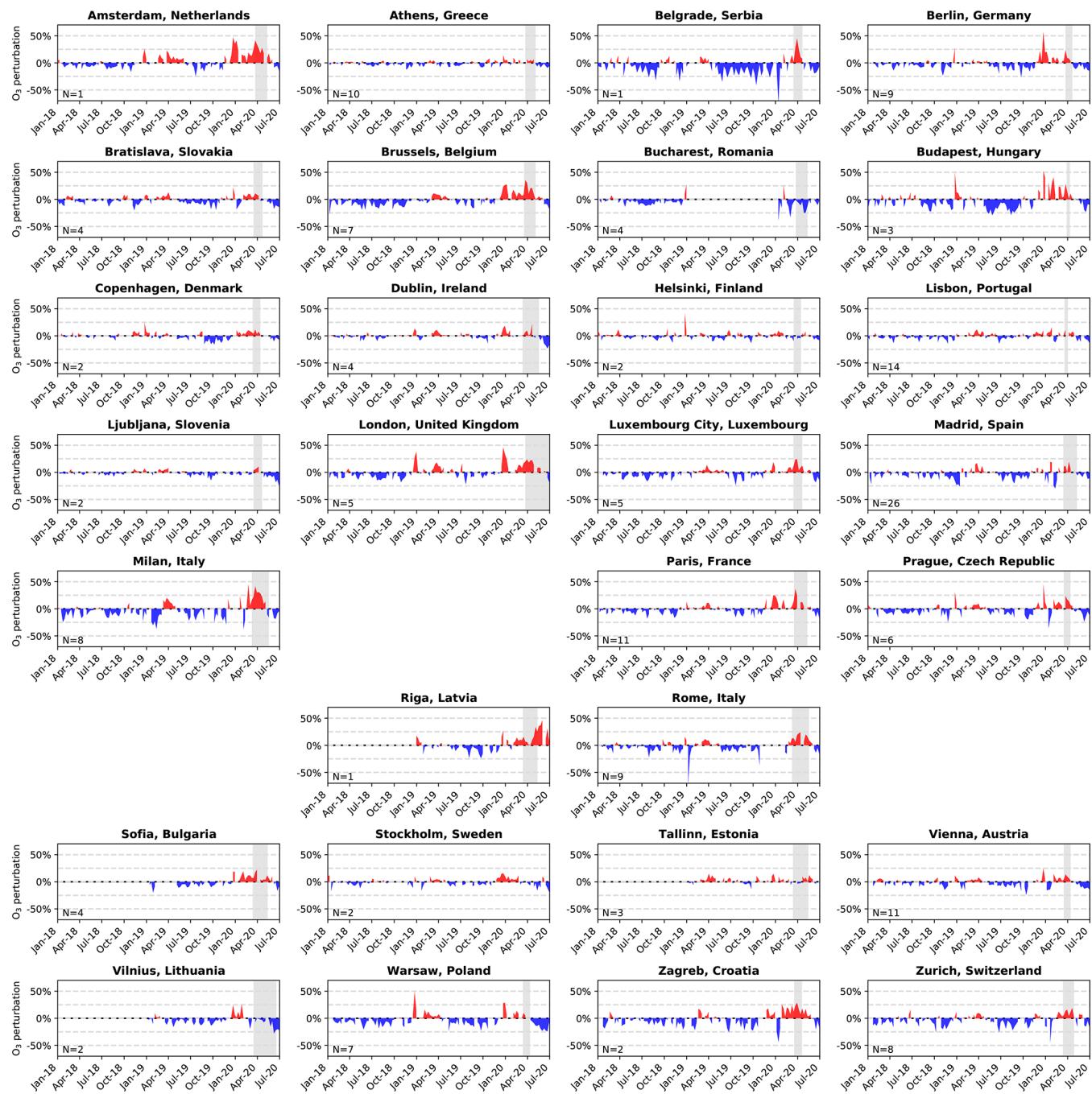
Figure A10. The same as Fig. A9 but for Europe. No observations are available for Reykjavik, Oslo, and Skopje.
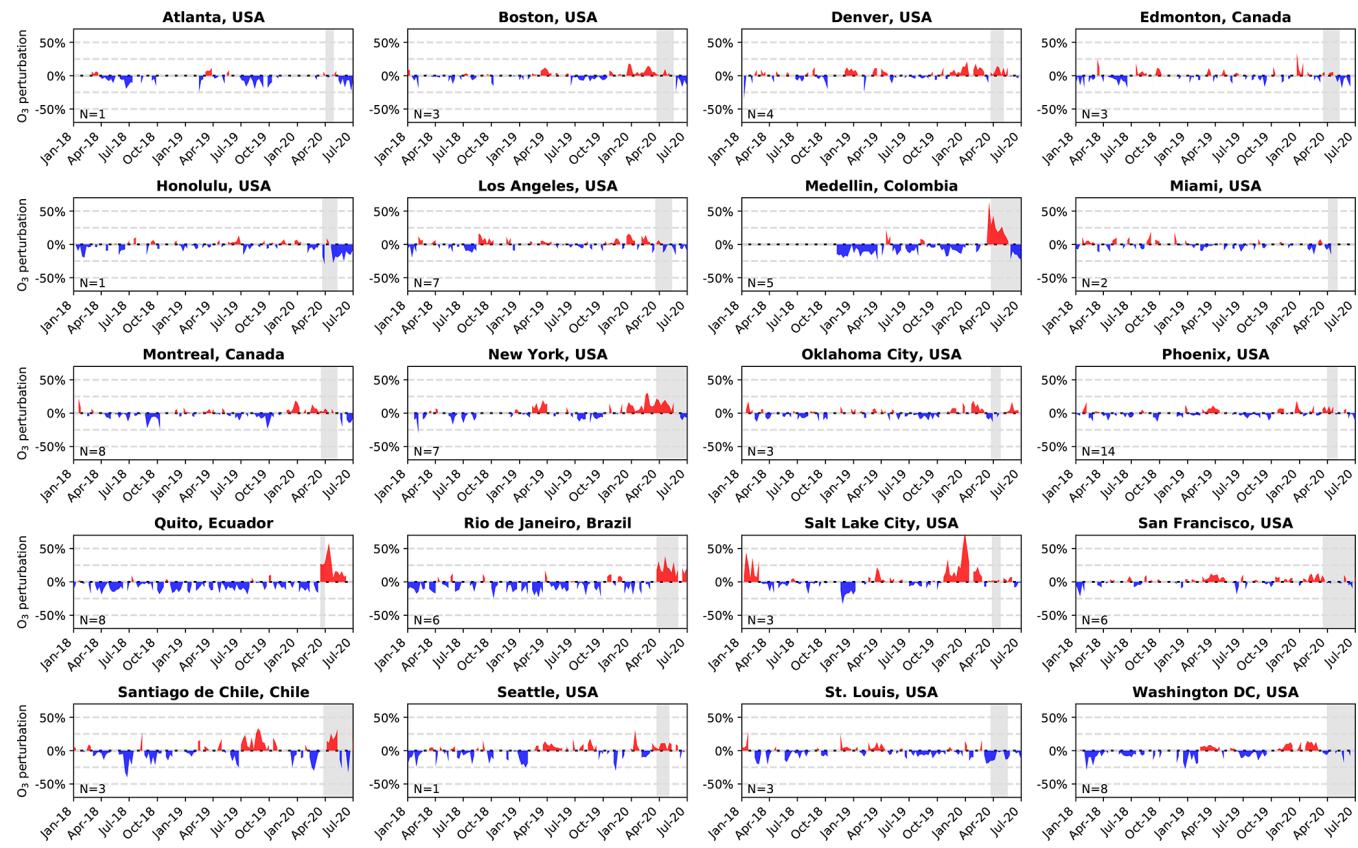
Figure A11. The same as Fig. A9 but for North America and South America.

Bias-corrected nitrogen dioxide normalized mean bias by local hour
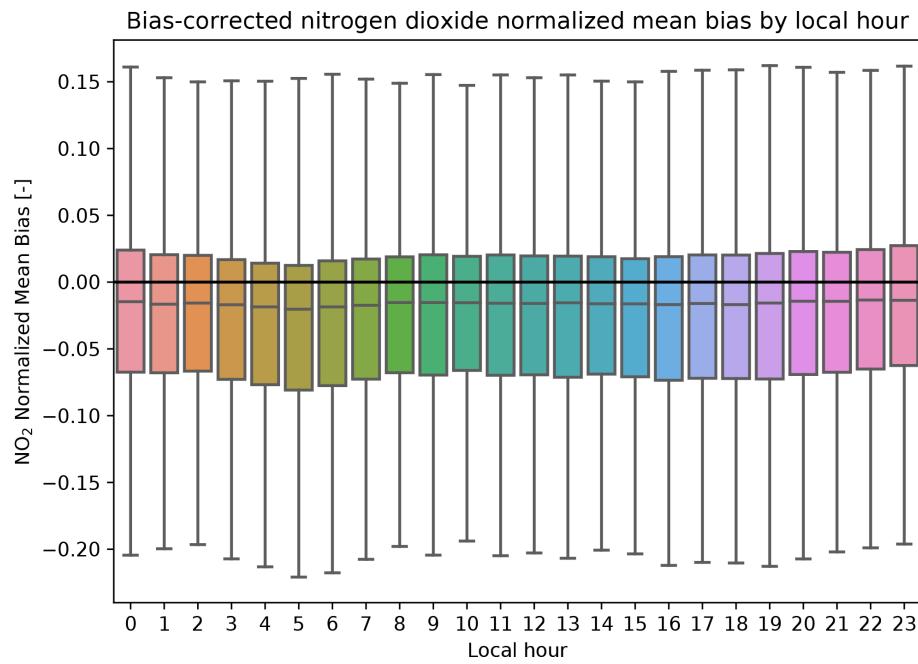
Figure A12. Distribution of normalized mean bias of the machine-learning-corrected nitrogen dioxide concentrations at all available observation sites as a function of local hour. Shown are the results for the test dataset.

Bias-corrected ozone normalized mean bias by local hour
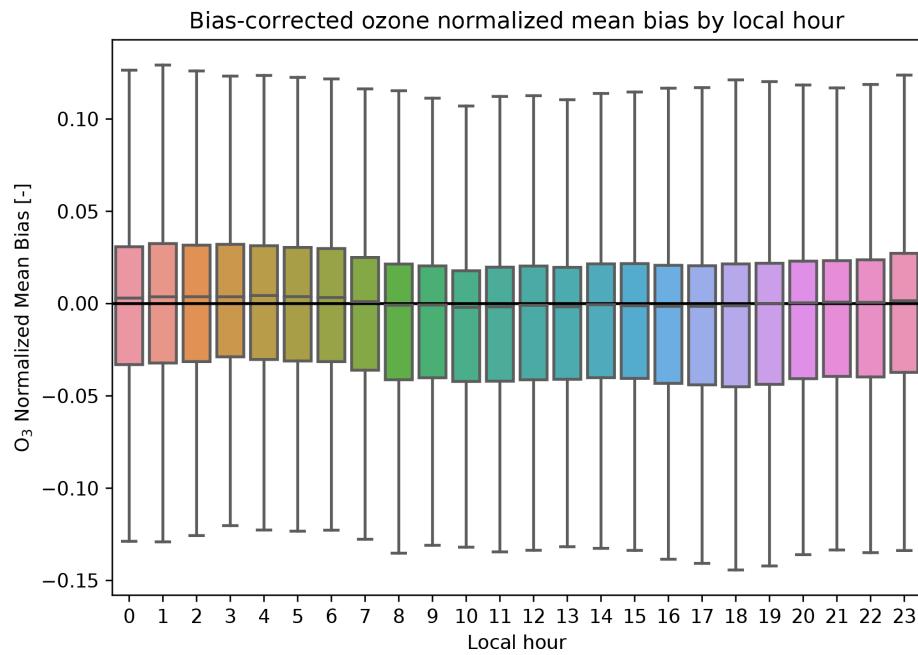
Figure A13. The same as Fig. A12 but for ozone.

Emission scale factors based on OMI NO$_2$ observations
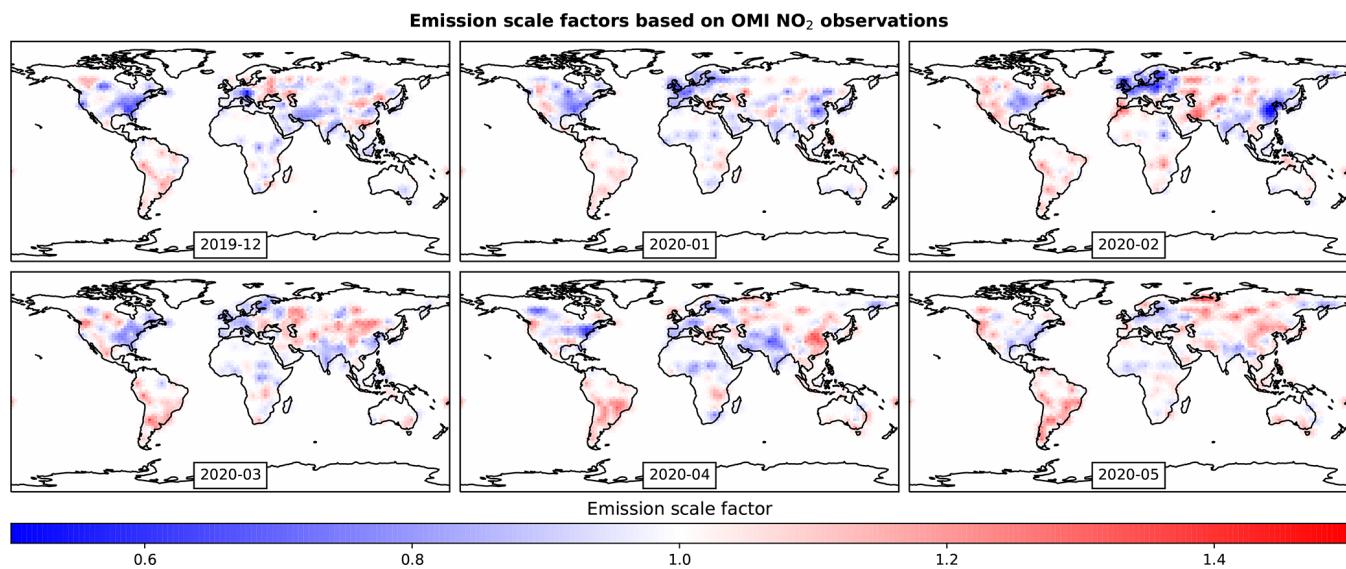
Figure A14. Emission scale factors used for model sensitivity simulation. Shown are the monthly average perturbations applied to the GEOS-CF anthropogenic base emissions.

References

Boersma, K. F., Eskes, H. J., Dirksen, R. J., van der A, R. J., Veefkind, J. P., Stammes, P., Huijnen, V., Kleipool, Q. L., Sneep, M., Claas, J., Leitão, J., Richter, A., Zhou, Y., and Brunner, D.: An improved tropospheric NO2 column retrieval algorithm for the Ozone Monitoring Instrument, Atmos. Meas. Tech., 4, 1905–1928, https://doi.org/10.5194/amt-4-1905-2011, 2011.

Castellanos, P. and Boersma, K.: Reductions in nitrogen oxides over Europe driven by environmental policy and economic recession, Sci. Rep., 2, 265, https://doi.org/10.1038/srep00265, 2012.

Chen, T. and Guestrin, C.: XGBoost: A Scalable Tree Boosting System, Proceedings of the 22nd ACM SIGKDD International Conference on Knowledge Discovery and Data Mining, August 2016, San Francisco California USA, 785–794, https://doi.org/10.1145/2939672.2939785, 2016.

Crippa, M., Solazzo, E., Huang, G., Guizzardi, D., Koffi, E., Muntean, M., Schieberle, C., Friedrich, R., and Janssens-Maenhout, G.: High resolution temporal profiles in the Emissions Database for Global Atmospheric Research, Sci. Data, 7, 121, https://doi.org/10.1038/s41597-020-0462-2, 2020.

Crippa, M., Guizzardi, D., Muntean, M., Schaaf, E., Dentener, F., van Aardenne, J. A., Monni, S., Doering, U., Olivier, J. G. J., Pagliari, V., and Janssens-Maenhout, G.: Gridded emissions of air pollutants for the period 1970–2012 within EDGAR v4.3.2, Earth Syst. Sci. Data, 10, 1987–2013, https://doi.org/10.5194/essd-10-1987-2018, 2018.

Dantas, G., Siciliano, B., França, B. B., da Silva, C. M., and Arbilla, G.: The impact of COVID-19 partial lockdown on the air quality of the city of Rio de Janeiro, Brazil, Sci. Total Environ., 729, 139085, https://doi.org/10.1016/j.scitotenv.2020.139085, 2020.

Darmenov, A. S. and da Silva, A.: The Quick Fire Emissions Dataset (QFED)–Documentation of versions 2.1, 2.2 and 2.4, Technical Report Series on Global Modeling and Data Assimilation, NASA//TM-2015-104606, Vol. 38, 212 pp., 2015.

Duncan, B. N., Lamsal, L. N., Thompson, A. M., Yoshida, Y., Lu, Z., Streets, D. G., Hurwitz, M. M., and Pickering, K. E.: A space-based, high-resolution view of notable changes in urban NOx pollution around the world (2005–2014), J. Geophys. Res. 121, 976–996, https://doi.org/10.1002/2015JD024121, 2016.

Frery J., Habrard A., Sebban M., Caelen O., and He-Guelton, L.: Efficient Top Rank Optimization with Gradient Boosting for Supervised Anomaly Detection, in: Machine Learning and Knowledge Discovery in Databases, edited by: Ceci, M., Hollmén, J., Todorovski, L., Vens, C., and Džeroski, S., ECML PKDD 2017, Lecture Notes in Computer Science, Vol. 10534, Springer, Cham, https://doi.org/10.1007/978-3-319-71249-9_2, 2017.

Friedman, J. H.: Greedy function approximation: A gradient boosting machine, Ann. Stat., 29, 1189–1232, https://doi.org/10.1214/aos/1013203451, 2001.

Grange, S. K. and Carslaw, D. C.: Using meteorological normalisation to detect interventions in air quality time series, Sci. Total Environ., 653, 578–588, https://doi.org/10.1016/j.scitotenv.2018.10.344, 2019.

Grange, S. K., Carslaw, D. C., Lewis, A. C., Boleti, E., and Hueglin, C.: Random forest meteorological normalisation models for Swiss PM$_{10}$ trend analysis, Atmos. Chem. Phys., 18, 6223–6239, https://doi.org/10.5194/acp-18-6223-2018, 2018.

Hilboll, A., Richter, A., and Burrows, J. P.: Long-term changes of tropospheric NO$_2$ over megacities derived from multiple satellite instruments, Atmos. Chem. Phys., 13, 4145–4169, https://doi.org/10.5194/acp-13-4145-2013, 2013.

Hu, L., Keller, C. A., Long, M. S., Sherwen, T., Auer, B., Da Silva, A., Nielsen, J. E., Pawson, S., Thompson, M. A., Trayanov, A. L., Travis, K. R., Grange, S. K., Evans, M. J., and Jacob, D. J.: Global simulation of tropospheric chemistry at 12.5 km resolution: performance and evaluation of the GEOS-Chem chemical module (v10-1) within the NASA GEOS Earth system model (GEOS-5 ESM), Geosci. Model Dev., 11, 4603–4620, https://doi.org/10.5194/gmd-11-4603-2018, 2018.

Ivatt, P. D. and Evans, M. J.: Improving the prediction of an atmospheric chemistry transport model using gradient-boosted regression trees, Atmos. Chem. Phys., 20, 8063–8082, https://doi.org/10.5194/acp-20-8063-2020, 2020.

Janssens-Maenhout, G., Crippa, M., Guizzardi, D., Dentener, F., Muntean, M., Pouliot, G., Keating, T., Zhang, Q., Kurokawa, J., Wankmüller, R., Denier van der Gon, H., Kuenen, J. J. P., Klimont, Z., Frost, G., Darras, S., Koffi, B., and Li, M.: HTAP_v2.2: a mosaic of regional and global emission grid maps for 2008 and 2010 to study hemispheric transport of air pollution, Atmos. Chem. Phys., 15, 11411–11432, https://doi.org/10.5194/acp-15-11411-2015, 2015.

Jhun, I., Coull, B. A., Zanobetti, A., and Koutrakis, P.: The impact of nitrogen oxides concentration decreases on ozone trends in the USA, Air Qual. Atmos. Health., 8, 283–292, https://https://doi.org/10.1007/s11869-014-0279-2, 2015.

Keller, C. A., Long, M. S., Yantosca, R. M., Da Silva, A. M., Pawson, S., and Jacob, D. J.: HEMCO v1.0: a versatile, ESMF-compliant component for calculating emissions in atmospheric models, Geosci. Model Dev., 7, 1409–1417, https://doi.org/10.5194/gmd-7-1409-2014, 2014.

Keller, C. A., Knowland, K. E., Duncan, B. N., Liu, J., Anderson, D. C., Das, S., Lucchesi, R. A., Lundgren, E. W., Nicely, J. M., Nielsen, J. E., Ott, L. E., Saunders, E., Strode, S. A., Wales, P. A., Jacob, D. J., and Pawson, S.: Description of the NASA GEOS Composition Forecast Modeling System GEOS-CF v1.0, Earth and Space Science Open Archive, p. 38, https://doi.org/10.1002/essoar.10505287.1, 2020.

Kleinert, F., Leufen, L. H., and Schultz, M. G.: IntelliO3-ts v1.0: a neural network approach to predict near-surface ozone concentrations in Germany, Geosci. Model Dev., 14, 1–25, https://doi.org/10.5194/gmd-14-1-2021, 2021.

Knowland, K. E., Keller, C. A., and Lucchesi, R.: File Specification for GEOS-CF Products, GMAO Office Note No. 17 (Version 1.1), 37 pp., available at: http://gmao.gsfc.nasa.gov/pubs/office_notes, last access: 4 July 2020.

Lamsal, L. N., Martin, R. V., Padmanabhan, A., van Donkelaar, A., Zhang, Q., Sioris, C. E., Chance, K., Kurosu, T. P., and Newchurch, M. J.: Application of satellite observations for timely updates to global anthropogenic NOx emission inventories, Geophys. Res. Lett., 38, L05810, https://https://doi.org/10.1029/2010GL046476, 2011.

Le, T., Wang, Y., Liu, L., Yang, J., Yung, Y. L., Li, G., and Seinfeld, J. H.: Unexpected air pollution with marked emission reductions during the COVID-19 outbreak in China, Science, 702–706, https://https://doi.org/10.1126/science.abb7431, 2020.

Le Quéré, C., Jackson, R. B., Jones, M. W., Smith, A. J. P., Abernethy, S., Andrew, R. M., De-Gol, A. J., Willis, D. R., Shan, Y., Canadell, J. G., Friedlingstein, P., Creutzig, F., and Peters, G. P.: Temporary reduction in daily global CO2 emissions during the COVID-19 forced confinement, Nat. Clim. Change, 647–653, https://doi.org/10.1038/s41558-020-0797-x, 2020.

Liu F., Page, A., Strode, S. A., Yoshida, Y., Choi, S., Zheng, B., Lamsal, L. N., Li, C., Krotov, N. A., Eskes, H., van der A., R., Veefkind, P., Levelt, P. F., Hauser, O. P., and Joiner, J.: Abrupt decline in tropospheric nitrogen dioxide over China after the outbreak of COVID-19, Sci. Adv., 6, 28, https://doi.org/10.1126/sciadv.abc2992, 2020a.

Liu, Z., Ciais, P., Deng, Z., Lei, R., Davis, S. J., Feng, S., Zheng, B., Cui, D., Dou, X., Zhu, B., Guo, R., Ke, P., Sun, T., Lu, C., He, P., Wang, Y., Yue, X., Wang, Y., Lei, Y., Zhou, H., Cai, Z., Wu, Y., Guo, R., Han, T., Xue, J., Boucher, O., Boucher, E., Chevallier, F., Tanaka, K., Wei, Y., Zhong, H., Kang, C., Zhang, N.,

Chen, B., Xi, F., Liu, M., Breon, F-M., Lu, Y., Zhang, Q., Guan, D., Gong, P., Kammen, D. M., He, K., and Schnellhuber, H. J.: Near-real-time monitoring of global CO2 emissions reveals the effects of the COVID-19 pandemic, Nat. Commun., 11, 5172, https://doi.org/10.1038/s41467-020-18922-7, 2020b.

Long, M. S., Yantosca, R., Nielsen, J. E., Keller, C. A., da Silva, A., Sulprizio, M. P., Pawson, S., and Jacob, D. J.: Development of a grid-independent GEOS-Chem chemical transport model (v9-02) as an atmospheric chemistry module for Earth system models, Geosci. Model Dev., 8, 595–602, https://doi.org/10.5194/gmd-8-595-2015, 2015.

Lucchesi, R.: File Specification for GEOS-5 FP-IT, GMAO Office Note No. 2 (Version 1.4) 58 pp., available at: http://gmao.gsfc.nasa.gov/pubs/office_notes.php (last access: 4 July 2020), 2015.

Lundberg, S. M. and Lee, S.-I.: A unified approach to interpreting model predictions, Adv. Neural Inf. Process. Syst., 30, 4768–4777, 2017.

Lundberg, S. M., Erion, G., Chen, H., DeGrave, A., Prutkin, J. M., Nair, B., Katz, R., Himmelfarb, J., Bansal, N., and Lee, S.-I.: From local explanations to global understanding with explainable AI for trees, Nat. Mach. Intell., 2, 56–67, https://doi.org/10.1038/s42256-019-0138-9, 2020.

Ministry of the Environment (MOE), Government of Japan: The Atmospheric Environmental Regional Observation System (AEROS), available at: http://soramame.taiki.go.jp/Index.php last access: 3 July 2020 (in Japanese).

Petetin, H., Bowdalo, D., Soret, A., Guevara, M., Jorba, O., Serradell, K., and Pérez García-Pando, C.: Meteorology-normalized impact of the COVID-19 lockdown upon NO2 pollution in Spain, Atmos. Chem. Phys., 20, 11119–11141, https://doi.org/10.5194/acp-20-11119-2020, 2020.

Russell, A. R., Valin, L. C., and Cohen, R. C.: Trends in OMI NO2 observations over the United States: effects of emission control technology and the economic recession, Atmos. Chem. Phys., 12, 12197–12209, https://doi.org/10.5194/acp-12-12197-2012, 2012.

Shah, V., Jacob, D. J., Li, K., Silvern, R. F., Zhai, S., Liu, M., Lin, J., and Zhang, Q.: Effect of changing NOx lifetime on the seasonality and long-term trends of satellite-observed tropospheric NO2 columns over China, Atmos. Chem. Phys., 20, 1483–1495, https://doi.org/10.5194/acp-20-1483-2020, 2020.

Seinfeld, J. H. and Pandis, S. N.: Atmospheric Chemistry and Physics: From Air Pollution to Climate Change, John Wiley & Sons, Hoboken, 2016.

Streets, D. G., Canty, T., Carmichael, G. R., de Foy, B., Dickerson, R. R., Duncan, B. N., Edwards, D. P., Haynes, J. A., Henze, D. K., Houyoux, M. R., Jacob, D. J., Krotkov, N. A., Lamsal, L. N., Liu, Y., Lu, Z., Martin, R. V., Pfister, G. G., Pinder, R. W., Salawitch, R. J., and Wecht, K. J.: Emissions estimation from satellite retrievals: A review of current capability, Atmos. Environ., 77, 1011–1042, https://doi.org/10.1016/j.atmosenv.2013.05.051, 2013.

Tobías, A., Carnerero, C., Reche, C., Massagué, J., Via, M., Minguillón, M. C., Alastuey, A., and Querol, X.: Changes in air quality during the lockdown in Barcelona (Spain) one month into the SARS-CoV-2 epidemic, Sci. Total Environ., 726, 138540, https://doi.org/10.1016/j.scitotenv.2020.138540, 2020.

Wargan, K., Pawson, S., Olsen, M. A., Witte, J. C., Douglass, A. R., Ziemke, J. R., Strahan, S. E., and Nielsen,

J. E.: The Global Structure of Upper Troposphere-Lower Stratosphere Ozone in GEOS-5: A Multi-Year Assimilation of EOS Aura Data, J. Geophys. Res.-Atmos, 120, 2013–2036, https://https://doi.org/10.1002/2014JD022493, 2015.